



UNIVERSITY OF TORONTO
FACULTY OF APPLIED SCIENCE & ENGINEERING

DEPARTMENT OF MATERIALS SCIENCE AND ENGINEERING

Thesis – MSE499Y

Hybrid Nanocrystalline Mesoscale Periodic Cellular Materials

Final Report

By
Lyle Gordon

Supervisor
Glenn Hibbard

A thesis submitted in conformity with the requirements for the Degree of Bachelor of Applied Science in the
University of Toronto

March 2008

Abstract

A new type of mesoscale periodic cellular material was developed by electrodepositing a high strength nanocrystalline nickel sleeve over a rapid prototyped acrylic photopolymer template. Mechanical properties of the hybrid-PCM, strength and stiffness, were measured in compression. For the thickest sleeves there was approximately a twenty times increase in the strength and stiffness of the trusses compared to the as-received polymer truss. Based on the mechanical properties of the constituent materials available analytical models were extended to predict the properties of the composite polymer-Ni PCM. The strength was predicted accurately based on the critical inelastic buckling stress of an individual strut. Scanning electron microscopy of truss samples revealed that that irreversible damage (failure of the nano-Ni sleeve over some of the face-sheet struts) began to occur only after the peak stress was reached. This observation was confirmed by the absence of small load drops in the pre-peak region of the stress-strain curve which are characteristic of cracking. In addition to the improved strength and stiffness due to the electrodeposited nano-Ni, the linear property scaling relationship characteristic of PCMs was observed for both strength and stiffness as a function of density.

Table of Contents

| | |
|---|----|
| Abstract..... | 1 |
| List of Figures | 4 |
| List of Tables | 6 |
| 1. Introduction | 7 |
| 2. Background | 11 |
| 2.1. Macroscale PCM Manufacturing..... | 11 |
| 2.1.1. Casting..... | 12 |
| 2.1.2. Deformation Forming..... | 12 |
| 2.1.3. Wire/Fiber/Textile based Approaches..... | 13 |
| 2.2. Mesoscale PCM Fabrication..... | 14 |
| 2.2.1. Rapid Prototyping | 15 |
| 2.2.2. Electrodeposition..... | 25 |
| 2.2.3 Self-Propagating Polymer Waveguides..... | 26 |
| 3. Experimental | 26 |
| 3.1. Rapid Prototyping | 27 |
| 3.2. Electrodeposition | 30 |
| 3.3. Coating Properties | 31 |
| 3.3.1. Thickness..... | 31 |
| 3.3.2. Grain Size | 31 |
| 3.4. Mechanical Testing | 32 |
| 3.5. Electron Microscopy | 32 |
| 4. Modeling | 33 |
| 4.1. Analytical Model | 35 |
| 4.1.1. Compressive Modulus..... | 35 |
| 4.1.2. Peak Compressive Stress..... | 37 |
| 4.2. Finite Element Analysis | 43 |
| 5. Results and Discussion | 46 |
| 5.1. Coating Properties | 46 |
| 5.1.1. Thickness..... | 46 |
| 5.1.2. Grain Size | 47 |
| 5.2. Electron Microscopy | 48 |
| 5.3. Compression Tests | 53 |
| 5.4. Compressive Modulus..... | 57 |
| 5.4.1. Finite Element Prediction..... | 59 |

| | |
|--|----|
| 5.5. Peak Compressive Strength | 60 |
| 5.5.1. Finite Element Prediction..... | 64 |
| 5.6. Scaling Relations | 66 |
| 5.7. Optimization | 69 |
| 6. Future Work | 75 |
| 7. Conclusion..... | 76 |
| References | 80 |
| Appendix A: Rapid Prototyping Datasheet | 84 |
| Appendix B: Wire Pre-form..... | 85 |
| Appendix C: Transverse shear corrected buckling stress | 87 |

List of Figures

| | |
|--|----|
| Figure 1: Various types of stochastic foams made by different manufacturing routes [3]. | 7 |
| Figure 2: Example of a stretch dominated PCM [1]. | 8 |
| Figure 3: Schematic Illustration of the Maxwell stability criterion in 2D. The pin-jointed frame (a) folds up under load; if the joints are welded the struts will experience bending. The triangulated pin-jointed frame (b) is stiff as the horizontal bar carries tensile load preventing bending, further; even if the joints are welded the frame would not weaken [1]. | 9 |
| Figure 4: Properties of Stretch-dominated lattices and bending-dominated foams compared to solid materials [1]. | 10 |
| Figure 5: Periodic cellular lattices with near optimal properties and single length scale [4]. | 10 |
| Figure 6: Investment Cast Cu-Be Alloy Microtruss [6]. | 12 |
| Figure 7: Deformation Formed Tetrahedral lattice PCM, cell size of 10mm [4]. | 13 |
| Figure 8: Kagome lattice microtruss woven from epoxy resin impregnated carbon fiber roving [14]. | 14 |
| Figure 9: Sub-millimetre scale micro-truss created using soft lithography and electrodeposition [7]. | 14 |
| Figure 10: Fractured PCM with sub-micron scale features created using holographic lithography [20]. | 15 |
| Figure 11: Sample PCM produced by Stampfl et al. using SLS. Scale bar is in centimetres [8]. | 16 |
| Figure 12: PCM produced by Santorinaios et al. using selective laser melting of stainless steel powder, 2.5 and 1.25 mm cell sizes. Technique similar to SLS except instead of sintering the powder below the melting point the powder is melted completely and resolidifies at the site of irradiation [24]. | 17 |
| Figure 13: Stereolithography Process Diagram [22]. | 18 |
| Figure 14: High resolution parts produced using microstereolithography [22]. | 19 |
| Figure 15: Illustration of Selective Laser Sintering Process [22]. | 20 |
| Figure 16: Laser Engineered Net Shaping Process [22]. | 21 |
| Figure 17: Inkjet based 3D Fabrication Process [22]. | 22 |
| Figure 18: 3D Printing Process Schematic [22]. | 23 |
| Figure 19: Extrusion-based Solid freeform Fabrication Process [22]. | 24 |
| Figure 20: Scanning electron micrograph of a truss produced from self-propagating photopolymer waveguides [35]. | 26 |
| Figure 21: Selected Mesoscale PCM Fabrication Methods. | 27 |
| Figure 22: Schematic diagram of pyramidal unit cell (a) and a cross-section of a constituent strut (b) having dimensions of strut length l , truss height h , strut thickness t , and truss angle ω [38]. | 28 |
| Figure 23: Rendering of CAD Model of Pyramidal Truss for Rapid Prototyping. | 30 |
| Figure 24: Assumed linearly elastic-perfectly plastic stress-strain plot for 3D Systems VisiJet HR. | 33 |
| Figure 25: True stress - true strain curve from a tensile test of nano-Ni (solid line) and Ramberg-Osgood fit (dashed line). | 34 |
| Figure 26: Composite strut cross-section, illustrating thickness (t) of nano-Ni plated on polymer core. | 36 |
| Figure 27: Plot of theoretical truss core modulus vs. thickness of electrodeposited nano-Ni. | 37 |
| Figure 28: Column curve for nano-Ni, critical stress for elastic (dashed line), inelastic (solid line) buckling and yield (dotted line) vs. slenderness ratio. The peak stresses of the experimentally tested samples are plotted against their respective slenderness ratios and fall in the range of inelastic buckling. | 41 |
| Figure 29: Theoretical peak stress over truss-area as a function of electrodeposited nano-Ni thickness. | 43 |
| Figure 30: Discretized geometry of entire truss with 122,057 linear 4 noded tetrahedral finite elements. | 45 |
| Figure 31: Non-linear finite element model of single unit cell. Mesh consists of 71,269 linear 4 noded tetrahedral elements. | 46 |

Figure 32: Representative optical micrograph of a ground and polished strut cross-section illustrating substrate and plating thickness variability. The thickness can be seen to vary more on the underside of the truss (shown on the top in this figure) due to contact with the support material during the rapid prototyping process. Node and strut section labeled on the cross-section 47

Figure 33: X-ray diffraction patterns for polycrystalline Ni standard (lower) and nanocrystalline Ni (upper). Peak broadening due to reduced grain size is apparent. Differences in relative peak intensity indicate the crystallographic texture of the sample. (Co-K α radiation $\lambda = 1.79 \text{ \AA}$). 48

Figure 34: Scanning electron micrograph of rough lower surface of as-received polymer truss..... 49

Figure 35: Scanning electron micrographs of the upper (a) and lower (b) surfaces of electrodeposited nickel on the truss illustrating the smooth (a) and rough (b) textures produced due to substrate roughness..... 49

Figure 36: SEM micrograph illustrating cracking which occurred in the diagonal corner struts of the face-sheet immediately after the peak load..... 50

Figure 37: (a) Scanning electron micrograph of sample after extensive compression showing the failure of an additional strut in the face-sheets and (b) magnified section of fracture surface of the failed face-sheet strut, the delamination of the nano-Ni from the polymer substrate is clearly evident, note the charging of the non-conductive polymer surface..... 51

Figure 38: (a) SEM micrograph showing the extensive buckling of the struts after continued deformation. (b) Individual buckled strut. The wrinkling in the strut is immediately evident as is the fact that the strut is no longer straight. Regions of local wrinkling and delamination are circled. 52

Figure 39: Micrograph which illustrates the global buckling of the strut on the left compared to the strut on the right which is still straight..... 52

Figure 40: Stress-strain curve for compression test of as-received polymer truss. Note the very low stress level over the plateau due to minimal ductility of the polymer. Displacements have been adjusted for machine compliance and strains are relative to entire truss height, 1.5mm..... 54

Figure 41: Full stress-strain curve for 45 μm thick nano-Ni plating sample. The five regions which make up the stress-curve are labeled on the curve the initial elastic linear region, the peak stress, the post-peak softening, the small plateau region and the densification region. Displacements have been adjusted for machine compliance and strains are relative to entire truss height, 1.5mm. 54

Figure 42: Sample stress-strain curves from compression testing of 5 trusses with increasing thicknesses of nano-Ni plating: 15, 26, 33, 40 and 45 μm . Increasing modulus and strength with increasing nano-Ni thickness is apparent. Displacements have been adjusted for machine compliance and strains are relative to entire truss height, 1.5mm. 55

Figure 43: (a) Failure occurring in the nano-Ni sleeves characterized by a series of nearly instantaneous load drops (indicated with arrows) visible in the post-peak region of the stress-strain curve. The inset figure highlights the region of interest plotted in the larger figure. (b) shows slope of tangent to stress strain curve – rapid decreases correlate with the load drops visible in (a). Sample has a plating thickness of 45 μm . Displacements have been adjusted for machine compliance and strains are relative to entire truss height, 1.5mm. 56

Figure 44: Slope of tangent to stress-strain curve as a function of strain from start of compression test to plateau region. Peak stress located at the first zero-crossing of the curve at a strain of approximately 14% (indicated with the arrow). The second zero-crossing indicates the plateau strain..... 57

Figure 45: Plot of measured modulus (points) along with theoretical prediction (solid line)..... 59

Figure 46: von Mises stress in full truss model (linear) after application of 0.015mm compressive displacement in the z-axis. Maximum stress of 11.4 MPa, deformation exaggerated by a factor of 18.8x. 60

Figure 47: Measured peak compressive stress (points) and theoretical peak compressive stress (solid line) as a function of plating thickness 62

| | |
|--|----|
| Figure 48: Stress-strain curve based on sum of top surface reaction forces and applied displacements to finite element model of single unit cell. The points represent individual time-points from the finite element analysis. | 64 |
| Figure 49: von Mises stress in single unit cell after application of a 0.3mm compressive displacement. The stress in the struts is equal to the yield stress of 32 MPa, note the extensive plastic deformation which occurs in the struts during compression. | 65 |
| Figure 50: Apparent truss core density as a function of electrodeposited nano-Ni coating thickness..... | 67 |
| Figure 51: Compressive modulus plotted as a function of density, points plotted represent experimental measurements for all trusses, and the solid line represents the linear regression..... | 67 |
| Figure 52: Peak compressive stress plotted as a function of density, points plotted represent experimental measurements for plated trusses, and the solid line represents the linear regression. | 68 |
| Figure 53: Comparison of strength of hollow struts compared to polymer filled struts – strength vs. density..... | 70 |
| Figure 54: Comparison of strength vs. density for trusses constructed from hollow and solid struts..... | 71 |
| Figure 55: Illustrating the effect of strut cross-section aspect ratio for a truss composed of solid struts. Strength/density increases with decreasing aspect ratio..... | 72 |
| Figure 56: Truss strength as a function of density for nano-Ni and poly-Ni plating..... | 73 |
| Figure 57: Specific strength plotted as a function of nano-Ni plating thickness. Individual points represent the experimental measurements and the continuous line is the theoretical prediction. | 74 |
| Figure 58: Specific modulus plotted as a function of nano-Ni plating thickness. Individual points represent the experimental measurements and the continuous line is the reduced theoretical modulus. | 74 |
| Figure 59: 2x2 Kagome Lattice Face-sheet drilling templates. | 86 |
| Figure 60: 2x2 Kagome Lattice Rendering | 86 |

List of Tables

| | |
|--|----|
| Table 1: Rapid Prototyped Truss Parameters (Theoretical)..... | 29 |
| Table 2: Selected Material Properties..... | 34 |
| Table 3: Predicted and measured compressive modulus for mesoscale truss structures along with nano-Ni coating thickness. The measured modulus is also expressed as a % of the theoretical value..... | 58 |
| Table 4: Predicted and measured peak strength for mesoscale truss structures along with nano-Ni coating thickness..... | 62 |

1. Introduction

There exists a distinction between two types of cellular solids [1]. Traditional manufactured foams, shown in Figure 1, along with the majority of biological cellular materials such as wood or bone [2]; either closed- or open-celled represent the first type, while, a second type known as periodic cellular materials also known as micro-trusses also exist, shown in Figure 2 [1]. The key distinction between the two is that during loading the individual struts which make up a traditional stochastic foam experience bending while micro-truss lattice structures are specifically engineered such that the struts experience only axial tensile or compressive forces [1].

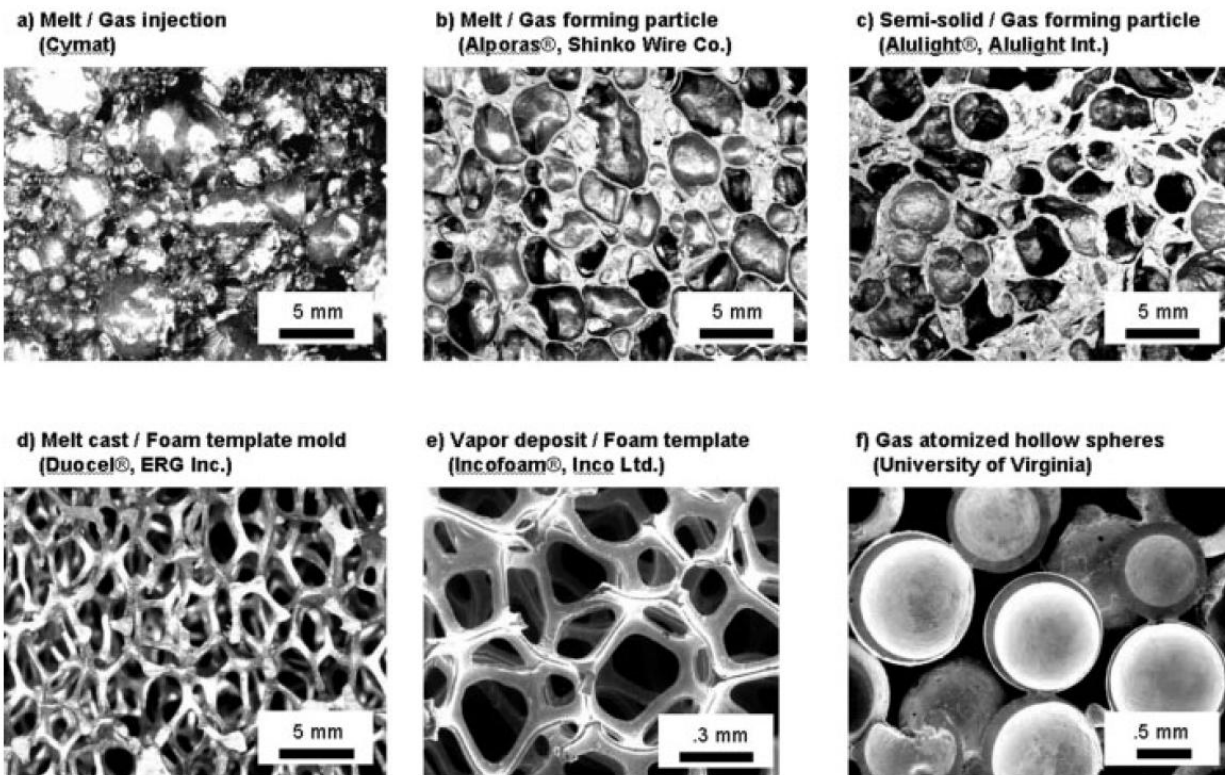


Figure 1: Various types of stochastic foams made by different manufacturing routes [3].

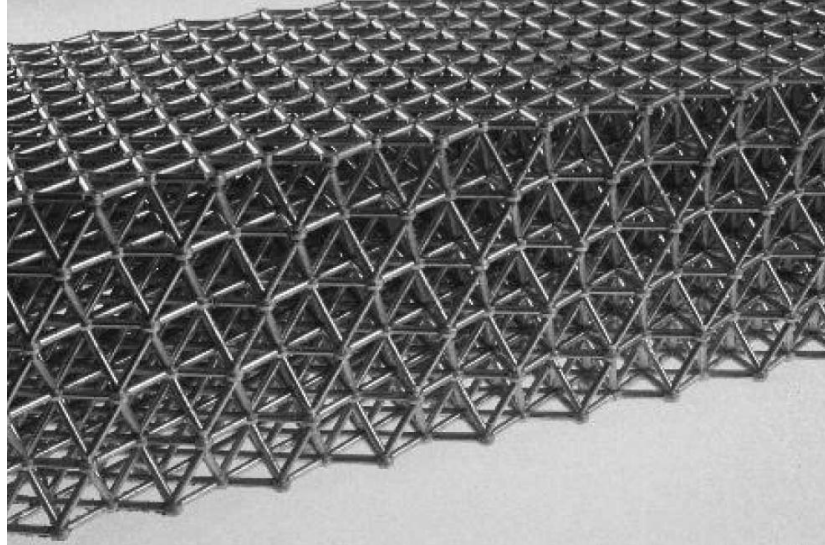


Figure 2: Example of a stretch dominated PCM [1].

The nature of stretch dominated lattices can be understood using the Maxwell stability criterion [1]. The Maxwell stability criterion states that for a statically determinate pin-jointed three dimensional frame, made up of b struts and j frictionless joints does not collapse if [1]:

$$M = b - 3j + 6 = 0$$

If the individual struts making up the frame are fixed then they will experience bending when the frame is loaded [1]. However, if $M > 0$, the struts will experience only tension or compression during loading even when pin-jointed, shown schematically in Figure 3 [1]. This is of critical importance to the efficient use of material as long and narrow structures are much stiffer and stronger in tension or compression than in bending, failing by inelastic buckling instead of in bending [1].

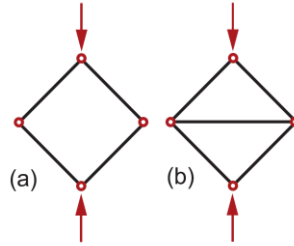


Figure 3: Schematic Illustration of the Maxwell stability criterion in 2D. The pin-jointed frame (a) folds up under load; if the joints are welded the struts will experience bending. The triangulated pin-jointed frame (b) is stiff as the horizontal bar carries tensile load preventing bending, further; even if the joints are welded the frame would not weaken [1].

Conventional bending-dominated foams have low stiffness and strength as their cell edges allow them to bend while novel stretch-dominated micro-truss lattices have greater stiffness and higher structural efficiency [1]. Figure 2 illustrates the relationship between stiffness and density for stretch-dominated lattices and bending dominated foams. It can be seen that the modulus of stretch-dominated lattices scales linearly with density while the modulus of bending-dominated foams scales with the square of density. The improved properties of the stretch-dominated lattices compared to bending dominated foams can be seen as the stretch-dominated lattices lie in a region above the bending-dominated foams.

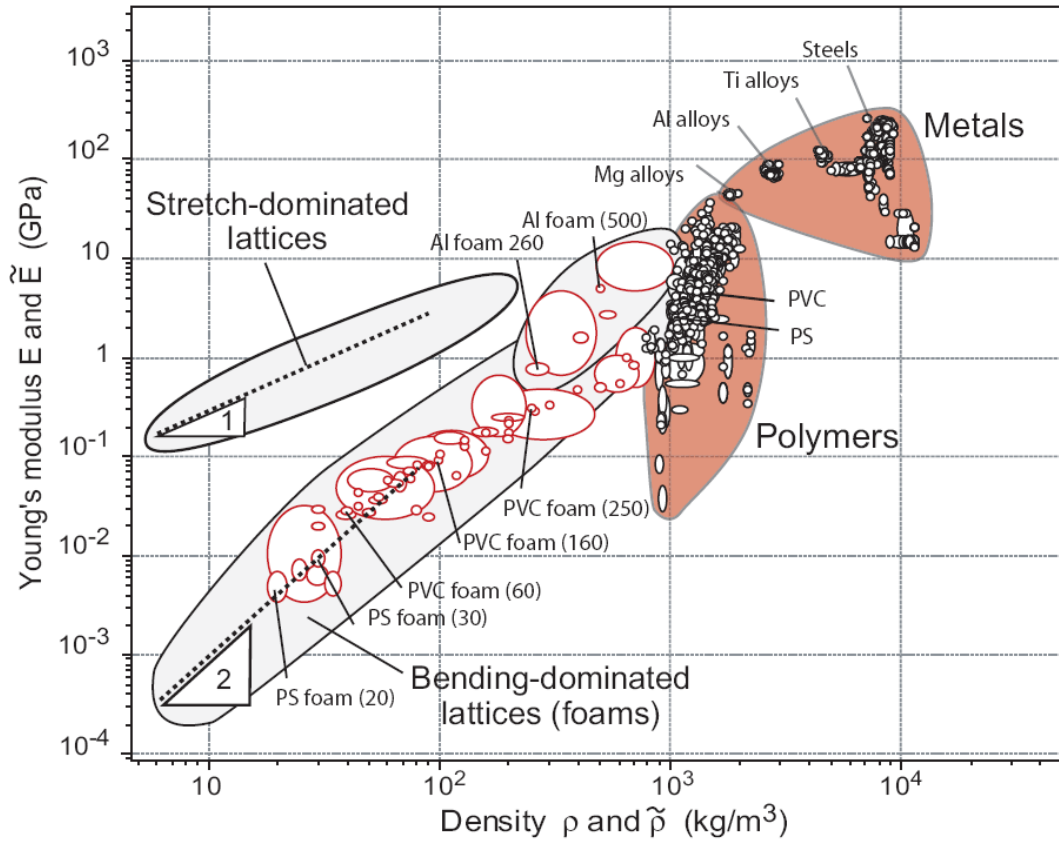


Figure 4: Properties of Stretch-dominated lattices and bending-dominated foams compared to solid materials [1].

Periodic cellular materials (PCM) with many different topologies have been shown to be effective as low weight core materials in composite sandwich structures [4]. PCMs with micro-truss architectures have been produced with adequate stiffness and strength with relative densities as low as 2% [1]. Figure 5 illustrates three lattices: the tetrahedral (a), pyramidal (b) and kagomé (c) lattice, each possesses near optimal mechanical properties, is stretch-dominated and has elements of only a single length scale [4].

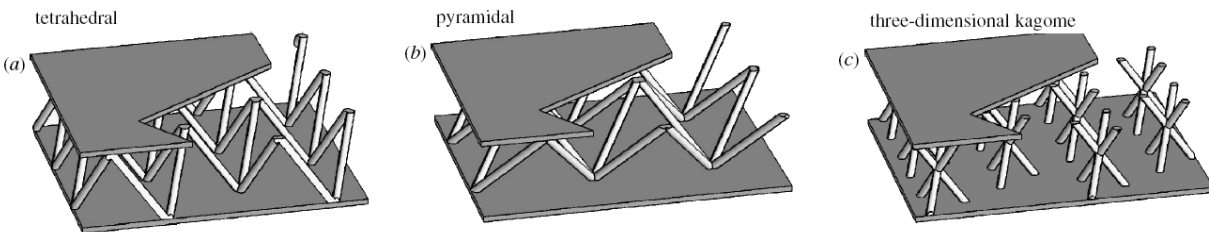


Figure 5: Periodic cellular lattices with near optimal properties and single length scale [4].

In addition to improved structural performance micro-truss PCMs exhibit a multitude of functionalities [4]. PCMs have been shown to have excellent energy absorption, thermal transport, fluid flow and acoustic insulation properties [4]. Due to the improved properties of micro-truss PCMs a wide range of future applications are possible. These applications include ultra-light structures, blast absorption systems, heat exchangers and acoustic insulation [5].

Although micro-truss PCMs have a wide array of possible applications the majority of PCMs presented in the literature have a strut length on the order of 10mm [1, 6]. Extending the micro-truss concept to much finer length scales on the order of 10s or 100s of microns (mesoscale) presents many new applications where lightweight multifunctional structures would be highly advantageous [7]. Possible small-scale applications of sub-millimeter scale PCMs include micro-air vehicles, space vehicles and robots, antennas, read/write arms in disk drives, MEMS components and biomedical devices with controlled pore geometry for regenerative medicine [7, 8]. In addition to the many small-scale applications, mesoscale PCM technologies would enable the production of very-thin sandwich structures with improved properties which could replace sheets of solid metal for use in land vehicle construction or air plane wing-skins [9]. Novel fabrication techniques or extensions of currently existing techniques will need to be devised to produce mesoscale micro-truss PCMs.

2. Background

2.1. Macroscale PCM Manufacturing

The majority of manufacturing methods which have been described to produce millimeter-scale PCMs involve traditional metal forming and fabrication technologies. The most commonly used methods are casting, deformation forming of expanded or perforated metal sheets and weaving of wires or fibers [6].

2.1.1. Casting

Casting micro-truss PCMs has been demonstrated using a rapid prototyped polymer form coated in ceramic slurry investment [6]. The polymer was then removed by melting or burn-out and a low viscosity molten casting alloy (e.g. Cu-Be or Al-Si) was poured into the mold. The high aspect ratio of the truss segments in optimal periodic structures present difficulties when casting, both limiting the choice of materials and introducing a considerable number of defects (ex. porosity) into the resulting PCM [6]. However, hot isostatic pressing (HIP) has been used successfully to reduce porosity following casting to produce higher strength PCMs from titanium alloy [10]. Figure 6 shows a kagomé lattice microtruss investment cast from a Cu-Be alloy. Overall, traditional casting methods produce a truss with a more limited range of properties, less than optimal structural efficiency, and relatively high cost. However, gel casting and slurry casting methods might enable the production of micro-trusses with fewer defects and higher aspect ratio out of a greater number of materials [6, 11].

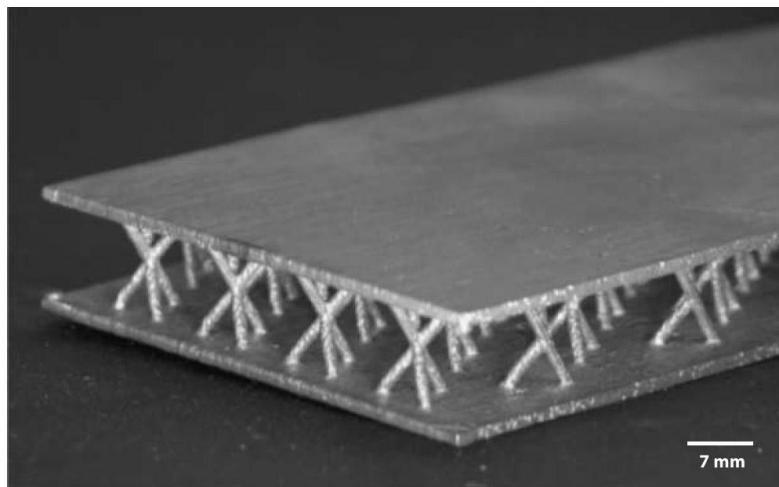


Figure 6: Investment Cast Cu-Be Alloy Microtruss [6].

2.1.2. Deformation Forming

Deformation forming has been widely used to produce various cellular topologies [6]. Most methods rely on deformation of a prefabricated or commercially produced perforated or expanded metal sheet to produce alternating nodes [6]. Different deformation modes, most commonly corrugation or

alternating out of plane deformation at the nodes, can be used to form PCMs with different architectures using perforated or expanded metal mesh [6, 3]. Following deformation the truss core is bonded to a solid or mesh face-sheet, commonly by brazing or resistance welding, to complete the PCM [3]. Figure 7 shows a tetrahedral lattice PCM assembled from perforated and corrugated metal. This method has been successfully scaled down to produce mesoscale trusses but becomes significantly more difficult at smaller scales [7].

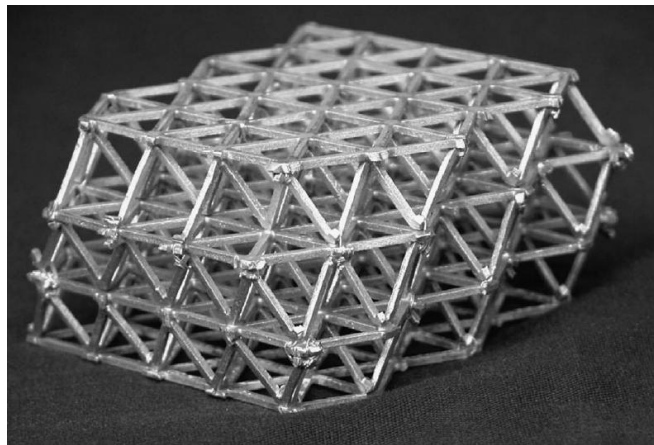


Figure 7: Deformation Formed Tetrahedral lattice PCM, cell size of 10mm [4].

2.1.3. Wire/Fiber/Textile based Approaches

Various techniques exist to produce PCMs using metal textiles, the simplest being simply bonding layers of woven or welded wire mesh to produce a periodic lattice [6]. This approach although simple and inexpensive does not produce a topologically optimal lattice [6]. More complex approaches based on weaving or bending of a single wire or fiber can be used to create topologically ideal lattices with improved properties [12, 13, 14, 15]. Figure 8 shows a kagomé lattice microtruss woven from epoxy resin impregnated carbon fiber roving through a pre-drilled face-sheet. Fabrication methods based on wires can potentially be scaled down to produce mesoscale PCM, however this requires adapting large scale, complex, and expensive weaving equipment to produce three dimensional structures. The reader is referred to [16] for more information on automated weaving of three dimensional textiles.

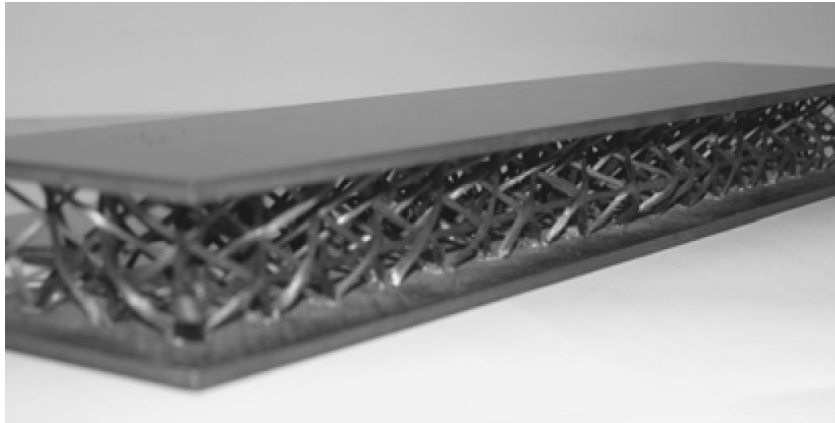


Figure 8: Kagome lattice microtruss woven from epoxy resin impregnated carbon fiber roving [14].

2.2. Mesoscale PCM Fabrication

Brittain et al. first described the production of a mesoscale PCM using a combination of soft-lithography and electrodeposition to produce a very fine ductile silver metal mesh with struts and openings on the order of 1mm. The silver mesh was then corrugated using a small custom brass die and nickel was electrodeposited over the silver to produce the mesoscale PCM [7]. Figure 9 shows the mesoscale PCM created by Brittain et al. This method provides an illustration of the possibilities of combining various well-developed microfabrication techniques (soft-lithography and electrodeposition) with existing micro-truss PCM fabrication methods (deformation forming) to produce mesoscale PCMs [7, 6, 17].

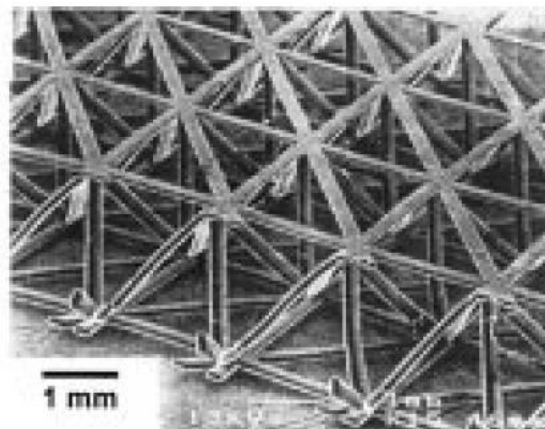


Figure 9: Sub-millimetre scale micro-truss created using soft lithography and electrodeposition [7].

In addition to PCMs, the importance of small scale periodic structures has been recognized in the field of photonics and has led to the development of many techniques to produce periodic structures with nanometer scale features known as photonic crystals [18, 19]. Photonic crystals have been produced using various microfabrication techniques based on top-down and bottom up methodologies [20]. Technologies described to form photonic crystals, such as colloidal crystal templating [18] or interference or holographic lithography [20, 21] are capable of producing exceptionally fine ordered microstructures but are limited in the overall size and volume of the end product they can produce and are not yet viable methods to create sub-millimeter scale PCMs. Figure 10 shows the level of detail which can be attained using holographic lithography.

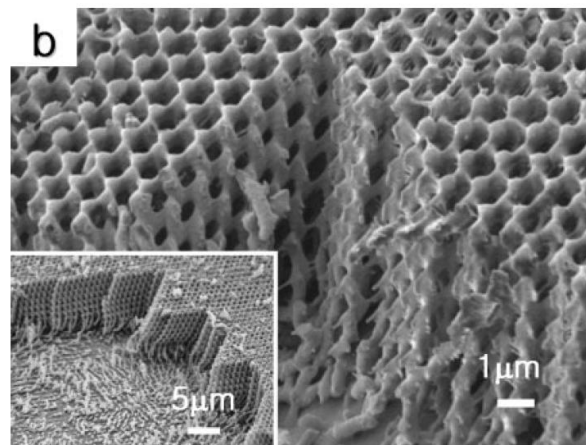


Figure 10: Fractured PCM with sub-micron scale features created using holographic lithography [20].

2.2.1. Rapid Prototyping

Many methods which have been described for PCM fabrication require deforming a perforated metal sheet out of plane to create alternating nodes [3]. This method has also been used by Brittain et al., as described above, to produce a mesoscale PCM; however, at smaller length scales it becomes increasingly difficult to deform the patterned metal sheets accurately [7]. Rapid prototyping prevents an alternative to the two step process of producing a sheet structure and then deforming it out of plane. Rapid prototyping technologies enable the rapid fabrication of accurate three dimensional physical

objects [22, 23]. In order to enable mesoscale PCM fabrication the selected technology must be able to fabricate heavily undercut models with easily removable support materials. The technology must also be capable of producing features with a resolution of approximately 100 μm .

Rapid prototyping technologies which can quickly produce an accurate three dimensional structure simplify the production of a mesoscale PCMs. Rapid prototyping has been used to create a polymer template to make a mold which was used to cast a metal PCM [6]. During casting the prototype was destroyed and the casting method itself is the limiting factor which controls the minimum length-scale of the PCM [6]. Stampfl et al. produced various mesoscale PCMs designed to replicate biological cellular materials using rapid prototyping technologies including selective laser sintering (SLS) and digital light projection (DLP), a variant of stereolithography (SLA). Figure 11 and Figure 12 show mesoscale PCMs produced using rapid prototyping technologies.

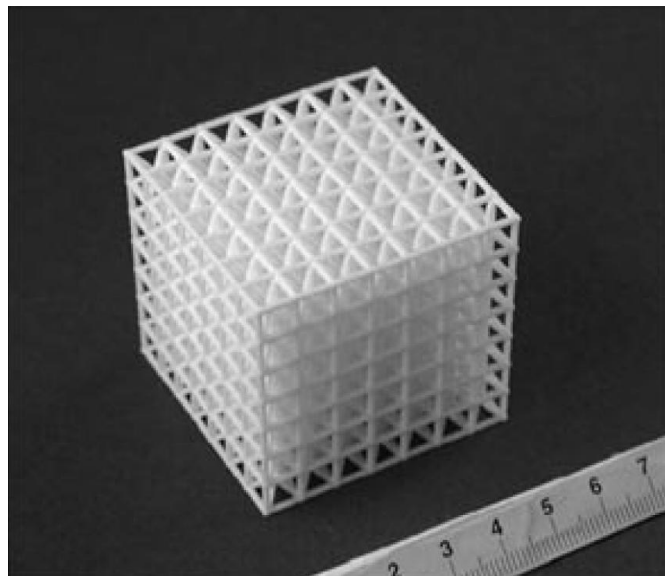


Figure 11: Sample PCM produced by Stampfl et al. using SLS. Scale bar is in centimetres [8].

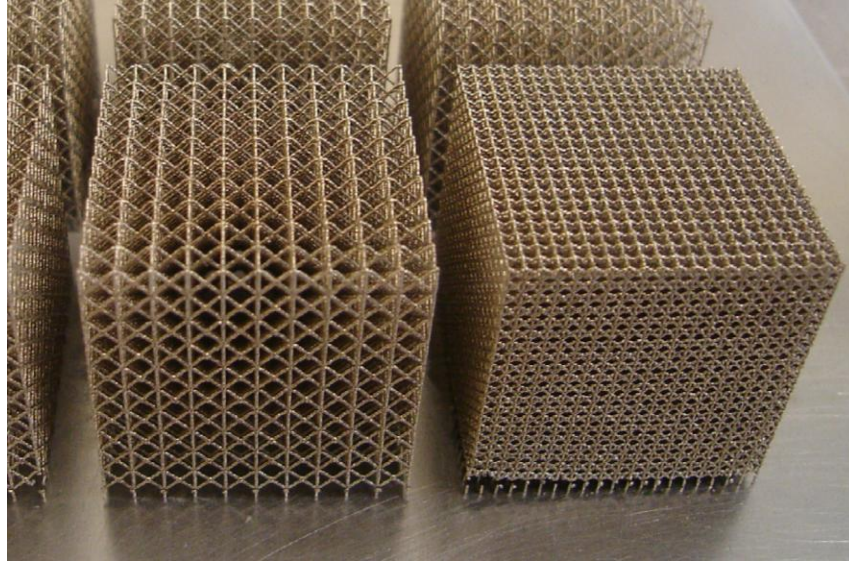


Figure 12: PCM produced by Santorinaios et al. using selective laser melting of stainless steel powder, 2.5 and 1.25 mm cell sizes. Technique similar to SLS except instead of sintering the powder below the melting point the powder is melted completely and resolidifies at the site of irradiation [24].

The four most common and well developed rapid prototyping methods, stereolithography (SLA), selective laser sintering (SLS), inkjet printing and extrusion techniques will be discussed here with relevance to mesoscale PCM fabrication [22].

2.2.1.1. Stereolithography

Stereolithography was the first rapid prototyping technology, developed by 3D Systems in 1984 [22]. Stereolithography involves the selective layer-by-layer solidification of a low-viscosity photoreactive polymer resin [22]. At the start of the process a platform is located just below the surface of a tank full of polymer resin containing a photoinitiator [22]. An ultraviolet laser then traces the geometry of the first slice of the model in the resin. The platform is then moved down a small distance and the laser solidifies the geometry of the second layer. This process repeats until the model is completed. Figure 13 illustrates the stereolithography process. The solidified part is then removed from the resin, excess resin washed off and the part is then cured by thermal or ultraviolet radiation. The accuracy of stereolithographically produced parts is limited by the following factors [22]:

- Resin composition
- Photoinitiator properties
- Laser beam properties (wavelength, intensity and beam diameter)
- Laser beam penetration and curing depth in resin
- X-Y accuracy of mirrors or laser
- Platform positioning accuracy in the z-direction

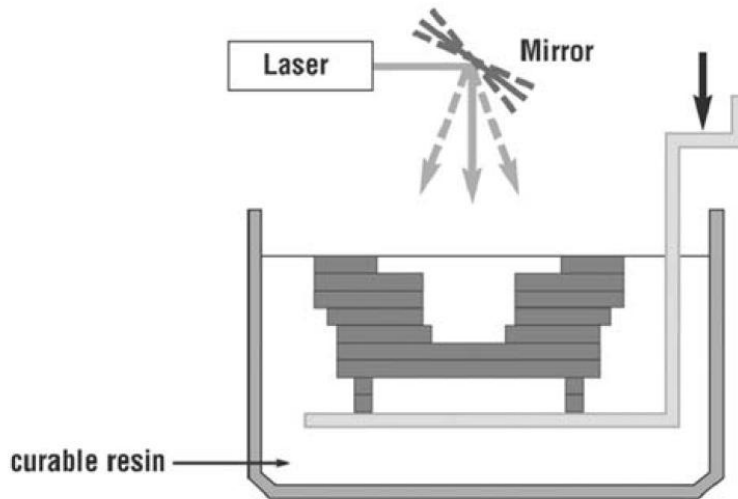


Figure 13: Stereolithography Process Diagram [22].

A modern high resolution SLA system (3D Systems Viper si2) has a $75\mu\text{m}$ beam diameter and a z-axis resolution of $2.5\mu\text{m}$ [25]. Theoretically this level of resolution would enable the production of sub-millimeter scale microtrusses. However, practically the production of microtrusses with commercially available SLA systems is difficult. The difficulty is due to the necessary cleaning before the part can be cured following laser solidification. Before post-curing the part is still very weak, however, supporting structures and excess photopolymer resin, which is relatively viscous, must be manually removed from the model [22]. Manually removing the supports and washing away the excess photopolymer resin often damages small $200\text{-}400\mu\text{m}$ diameter features [26]. If the part is not adequately cleaned excess resin will solidify during the post-curing step, altering the geometry of the model.

Further miniaturization of the structures producible with stereolithography has been made possible by a redesign of the stereolithography machine [22]. Instead of scanning the laser beam directly over the surface of the resin the laser is instead passed through a pattern generator such as a transmissive mode liquid crystal display or a MEMS micro-mirror device (also known as digital light projection, DLP [8]). This change not only allows for the entire resin surface to be exposed simultaneously which improves the speed but enables selective polymerization of one volume element (voxel) without affecting surrounding areas, increasing resolution [22]. This technique, known as microstereolithography, would be capable of producing high resolution micro-truss models but the technology is not yet widely available. Figure 14 illustrates the level of detail available with microstereolithography.

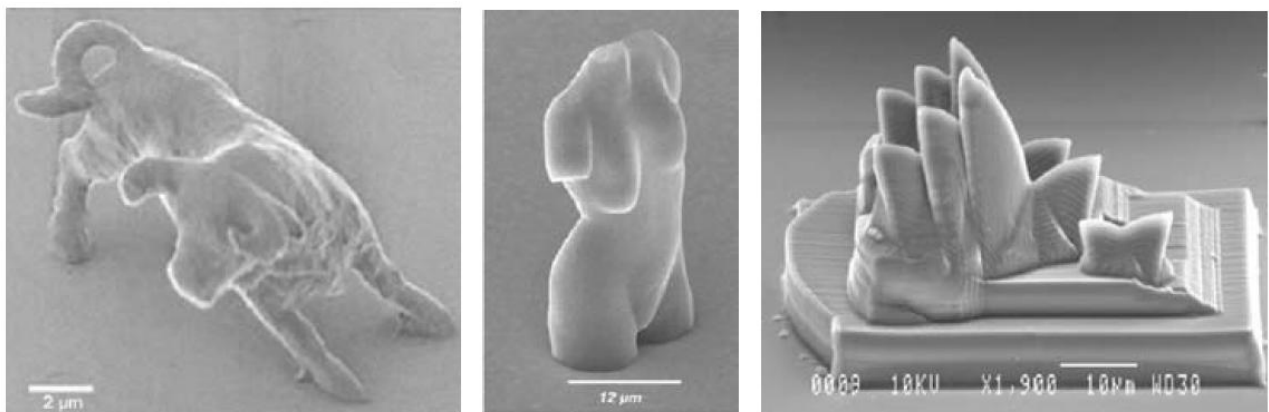


Figure 14: High resolution parts produced using microstereolithography [22].

Many other technologies, such as holographic lithography and interference lithography, rely on photopolymerization of resins to build three dimensional structures [22, 20, 19, 27, 21]. Combining these freeform volume fabrication technologies (illustrated in Figure 10), which are well suited to producing periodic structures, with microstereolithography presents an as yet unexplored method of producing fine scale periodic materials with a larger overall size than is currently possible using interference/holographic lithography alone.

2.2.1.2. Selective Laser Sintering

Selective laser sintering (SLS) works by joining powder particles selectively using a laser beam [22].

During each step of the process a thin layer of powder is spread out and then a laser traces a pattern in the powder, selectively sintering the powder by heating to just below the powder's melting point [22].

The lower platform then moves down and another layer of powder is spread out over the existing structure. These steps are repeated until fabrication is completed. The part is then removed and excess un-sintered powder, which supported the model during sintering, is cleaned off [22]. Figure 15 illustrates the SLS process.

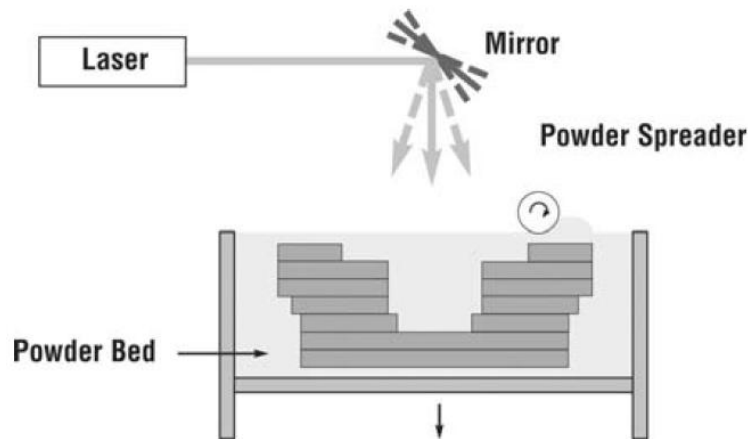


Figure 15: Illustration of Selective Laser Sintering Process [22].

Another technology, known as laser engineered net shaping (LENS) is similar to SLS, except instead of each layer of powder being spread out on top of the previous layers the powder is ejected from a nozzle into the focal point of the laser [22]. Figure 16 illustrates the LENS process.

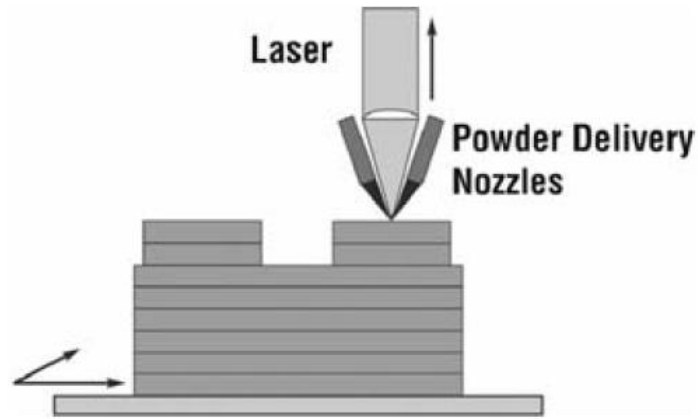


Figure 16: Laser Engineered Net Shaping Process [22].

Accuracy of laser sintering fabrication methods is limited by the laser beam diameter and the powder size. Unlike SLA, which produces a relatively smooth surface finish on completed parts, during SLS powder particles adhere to the surface of the part leaving a rough surface which needs to be sanded smooth [22]. The benefit of SLS is the wide range of possible materials including metals; however, the attainable feature resolution is not as good as other methods. Although the technology is capable of producing a mesoscale PCM SLS does not possess the accuracy necessary to create the fine-scale sub-millimeter features desired for this work [22, 8].

2.2.1.3. Inkjet Printing

Inkjet printing technology was developed for printing two dimension images or text on paper [22]. The process involves ejecting tiny droplets of ink onto the page [22]. Extending the technology to produce three dimensional models involved changing from depositing ink to directly depositing polymer droplets. Initially inkjet method machines used melted thermoplastic droplets and a wax for the supports which were ejected selectively to form the model layer by layer [22]. After each layer was deposited the layer thickness was milled to the correct height prior to depositing the next layer. Recently, UV curing photopolymers have replaced thermoplastics; each layer is deposited and then cured under a UV light source [22]. The accuracy of the process is limited by the droplet size, the

positioning accuracy of the printhead and the layer thickness which can be milled. The highest resolution commercially available inkjet modeling system is the 3D Systems InVision HR, which uses multi-jet modeling (MJM), is capable of a resolution of $38\mu\text{m}$ in the x-y plane and a minimum layer thickness of $30\mu\text{m}$ [28], the highest in-plane resolution of any of the commonly available solid freeform fabrication methods. Figure 17 illustrates the inkjet modeling process, without the UV curing step.

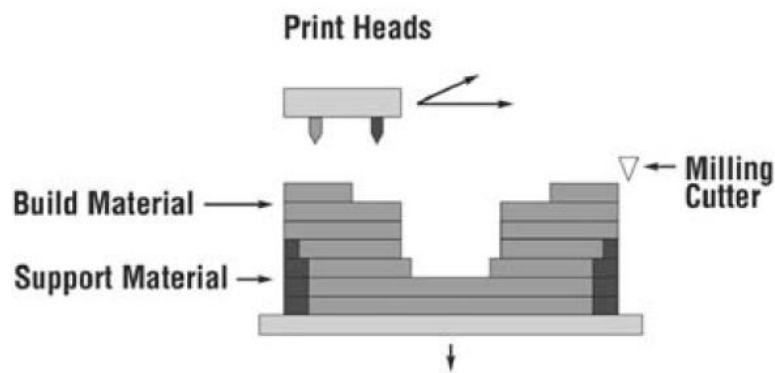


Figure 17: Inkjet based 3D Fabrication Process [22].

Another technology also based on inkjet printing is known as 3D printing (3DP) [22]. 3DP involves spreading individual layers of ceramic or polymeric powder and then selectively joining the powder by depositing droplets of liquid binder from a print-head. This method is able to produce parts quickly and inexpensively however the accuracy and surface finish is not as good as direct inkjet methods [22].

Figure 18 illustrates the 3DP process.

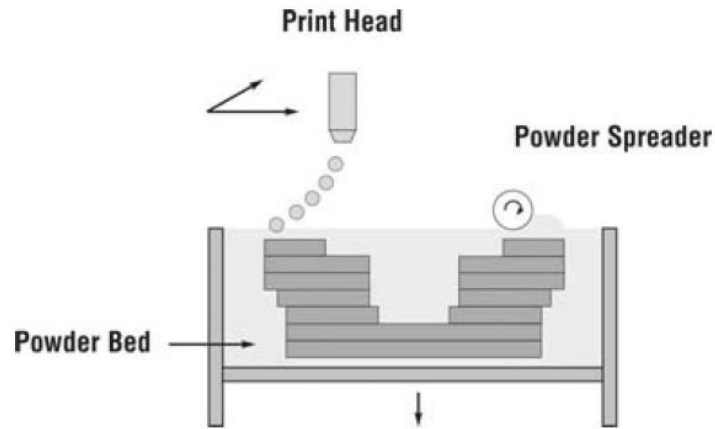


Figure 18: 3D Printing Process Schematic [22].

2.2.1.4. Extrusion Techniques

Unlike inkjet printing methods which deposit droplets of material individually, extrusion based methods deposit a continuous stream of molten material to build the model [22]. A filament of material, most commonly acrylonitrile-butadiene-styrene copolymer, is passed through a heated nozzle where the material is melted [22]. The molten material then deposits as a continuous bead. The accuracy of extrusion methods is limited by the diameter of the nozzle and currently resolutions of only 250-1000 μm are attainable commercially making it unsuitable for sub-millimeter scale PCM fabrication. Figure 19 illustrates the extrusion modeling process.

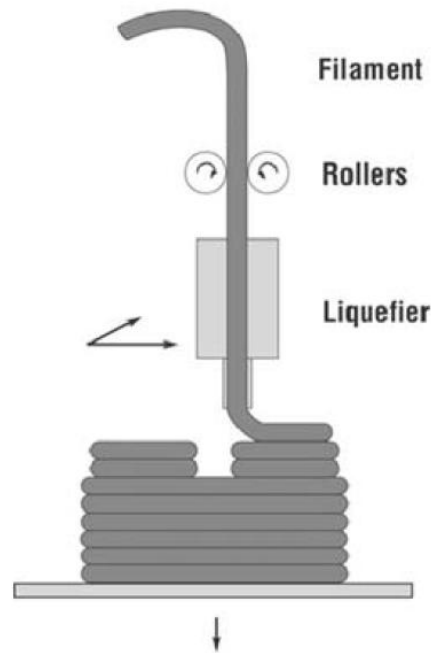


Figure 19: Extrusion-based Solid freeform Fabrication Process [22].

Commercially available rapid prototyping technologies which exhibit the necessary accuracy to produce mesoscale PCMs, SLA and MJM, can currently only create polymer templates [22]. These polymer templates have low strength and low stiffness compared to metals [22]. To solve this problem Wadley et al. used the rapid prototyped model as a template for casting, which destroys the template [6]. The possibility of incorporating metal or ceramic particles in the polymer part followed by sintering to remove the polymer and create a dense high-strength part has also been demonstrated [8, 22]. However, instead of destroying the prototype by using it to create a mold for casting, the prototype can be coated with a high strength material to create a composite part with increased strength and stiffness compared to the as-prototyped polymer. Electrodeposition is a method capable of depositing high strength material, encapsulating the low strength polymer template, and is able to resolve the sub-millimeter structures present on the prototype [29].

2.2.2. Electrodeposition

Micro-truss structures represent novel materials able to fill gaps in the material property space by providing higher strength and stiffness at lower density [1]. However, it is currently difficult to produce mesoscale PCMs from high strength and high stiffness materials. By combining a high resolution rapid prototyped polymer model with electrodeposition it has been found to be possible to create a high strength composite PCM.

Nanocrystalline metal presents an ideal material to electrodeposit over a low strength polymeric template [30, 29]. Nanomaterials with grain sizes on the order of 5 to 100 nm have increased yield strength due to a large volume fraction of intercrystalline material [30]. The increased strength is understood based on Hall-Petch strengthening as the increased volume of grain boundaries impedes dislocation motion [30].

Electrodeposition has been shown to be able to economically produce nanostructured metals [29]. However, even more importantly, electrodeposition has been shown to be an effective method to produce metal structures with very fine detail, demonstrated by its long use in the microfabrication industry, for example for the fabrication of microelectromechanical systems (MEMS) and honeycomb microcomposites [31, 32]. The ability to produce high-strength structures with micron-level resolution is necessary for mesoscale PCM fabrication. Suralvo et al. have shown that electrodeposition of a nanocrystalline metallic sleeve over a three-dimensional truss template, which provides the structure of the PCM, is capable of producing significantly higher strength micro-trusses [33]. Not only is the electrodeposited metal stronger and stiffer than the template but by placing it further away from the central axis of the strut its structural efficiency is enhanced, analogous to the improvement gained from using a wide hollow tube instead of a narrow solid rod to prevent buckling [34].

2.2.3 Self-Propagating Polymer Waveguides

An alternative method for producing mesoscale PCMs which is superficially similar to SLS is the method Jacobsen et al. developed to rapidly (< 1 min) produce thick (> 5 mm) mesoscale trusses using self-polymerizing photopolymer waveguides [35]. Upon exposing the top surface of a photopolymer resin to a specific pattern of UV light polymerization occurs in the exposed regions [35]. The light then becomes trapped in the polymerized region forming a waveguide that continues to propagate into the resin due to internal reflection [35]. By modifying the pattern through which the resin is exposed and the geometry of the resin container they can adjust the geometry of the truss [35]. Jacobsen et al. have since published experimental compressive and shear properties of these trusses along with accurate predictions of their properties [36, 37]. Figure 20 shows a micrograph of one of the trusses produced by Jacobsen et al. using self-propagating photopolymer waveguides.

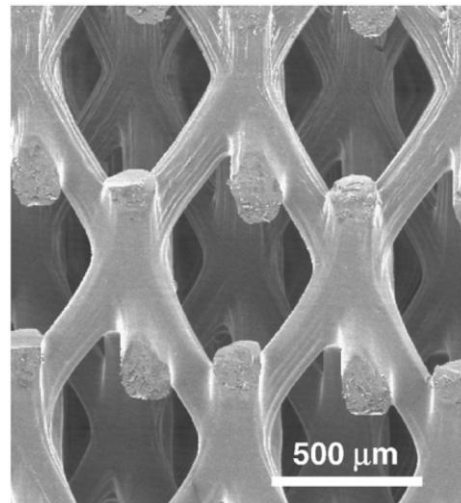


Figure 20: Scanning electron micrograph of a truss produced from self-propagating photopolymer waveguides [35].

3. Experimental

Production of mesoscale PCMs requires developing novel fabrication methods capable of creating the truss structures at much small length scales. Preliminary research focused on two different fabrication methods, both based on fabricating a three dimensional structure with an optimal microtruss geometry

and then depositing a sleeve of nanocrystalline metal on to the pre-formed template to provide strength and rigidity. Figure 21 lists some possible approaches for fabrication of mesoscale PCMs, including the primary method explored in this study (**bolded**).

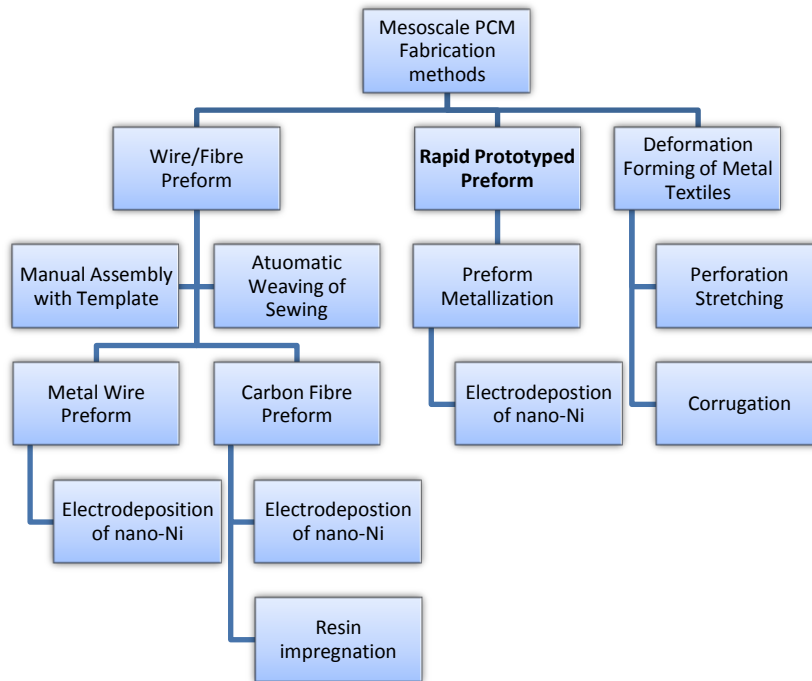


Figure 21: Selected Mesoscale PCM Fabrication Methods

The initial (unsuccessful) method explored in this study which involved the electrodeposition of a pre-form fabricated by sewing or weaving a fine metallic wire through a pre-drilled template is described in Appendix B. The second method involved the electrodeposition of a multi-jet-modeling rapid prototyped polymer template is described below.

3.1. Rapid Prototyping

The mesoscale PCM, produced by Brittaun et al. required mechanical deformation of the electrodeposited silver template by hand prior to assembly [7]. Precise deformation of the metal sheet becomes increasingly difficult and time consuming at small length scales. By taking advantage of the ability of existing commercialized rapid prototyping technology to build high resolution three

dimensional structure from the bottom up the difficult deformation step can be skipped. Multi-jet modeling, a method of direct droplet 3D inkjet printing with multiple nozzles was selected as it produced the necessary level of resolution, was relatively inexpensive, and was commercially available [22].

A computer aided design (CAD) model of a 17.8 x 17.8 x 1.5mm pyramidal truss (including top and bottom face-sheet) (Figure 5b) was prepared using Autodesk Inventor (Autodesk Inc, San Rafael, CA).

Truss parameters are outlined in

Table 1. The truss geometry is illustrated in (Figure 22). The model was converted into a STL file which represents the model as a set of triangulated surfaces for sending to the rapid prototyping firm. Figure 23 is a rendering of the mesoscale truss. The STL file was sent electronically to FineLine Prototyping (Raleigh, NC) where it was fabricated on a 3D Systems InVision HR 3-D Modeler (3D Systems Inc, Rock Hill, SC) using a proprietary acrylic photopolymer, VisiJet HR (3D Systems Inc, as before). Physical and chemical properties for the resin and the cured polymer (provided by the manufacturer) are included Appendix A.

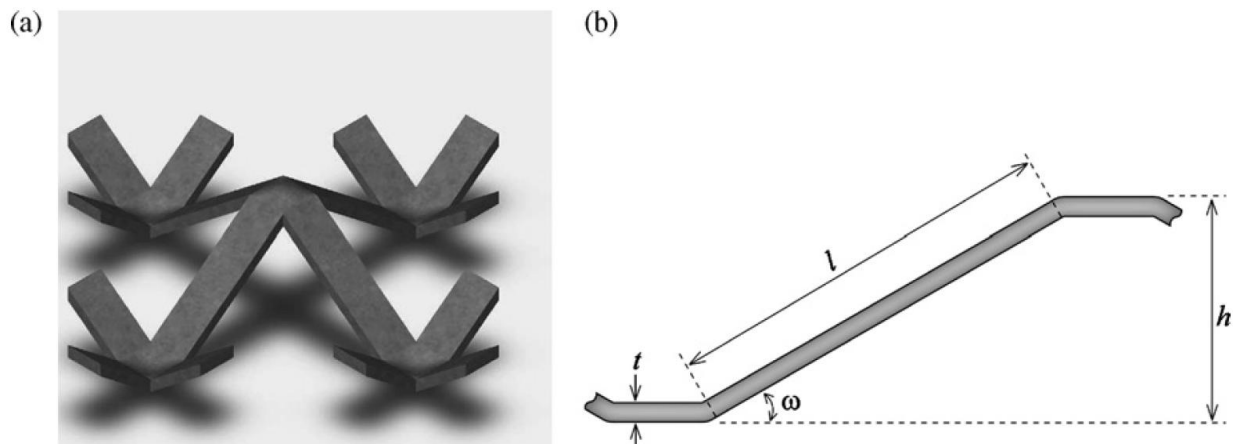


Figure 22: Schematic diagram of pyramidal unit cell (a) and a cross-section of a constituent strut (b) having dimensions of strut length l , truss height h , strut thickness t , and truss angle ω [38].

Table 1: Rapid Prototyped Truss Parameters (Theoretical)

| | |
|--|--|
| Lattice type | Pyramidal |
| Strut length (l) | 1.38 mm |
| Face-sheet thickness | 260 μm |
| Strut cross-section | Rectangular |
| Strut width (w) | 390 μm |
| Strut thickness (t) | 180 μm |
| Strut cross-sectional area | 0.07 mm^2 |
| Strut volume | 0.097 mm^3 |
| Total truss height (h) | 1.5 mm |
| Truss core height | 0.98 mm |
| Truss core volume | 310.5 mm^3 |
| Truss core volume fraction (V_f) | 4.5% |
| Strut angle (ω) | 45° |
| Number of struts | 144 |
| Base dimensions | Square: 17.8 x 17.8 mm |
| Projected base area | 316.84 mm^2 |
| Total surface area | 710.18 mm^2 |
| Material | 3D Systems VisiJet HR 200 Acrylic-type photopolymer |

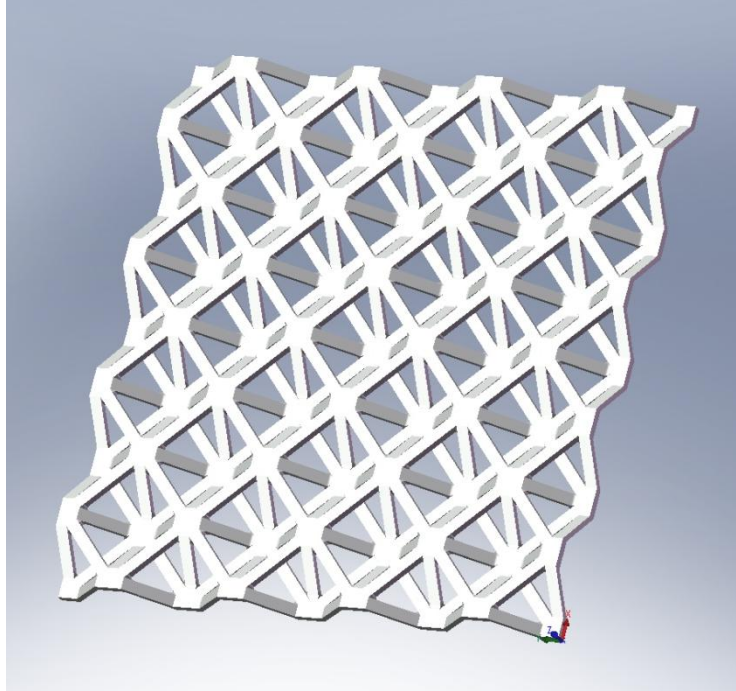


Figure 23: Rendering of CAD Model of Pyramidal Truss for Rapid Prototyping.

3.2. Electrodeposition

Electrodeposition requires that the substrate to be plated is electrically conductive. Since the rapid prototyped polymer template is non-conductive it was metalized using a proprietary process before being plated. It can be seen in Figure 23 that the top face-sheet of the rapid prototyped truss was rotated 45° with respect to the bottom face-sheet. This was done to minimize shielding effects during electrodeposition. Electrodeposition of nanocrystalline metal was done using a procedure similar to that described by Cheung et al. [39] at Integran Technologies (Toronto, Ontario). First a thin layer of copper was plated onto the metalized polymer and then the specified thickness of nickel was deposited.

3.3. Coating Properties

3.3.1. Thickness

3.3.1.1. In-direct: weight based method

Initially, a set of 12 of the as-received rapid prototyped samples were weighed to the nearest 0.1 mg. The variability in the masses of the individual as-received trusses was found to be very small and for later calculations the average mass of the initial sample was used. Following plating the samples were weighed again and the initial weight was subtracted from the new weight, giving the mass of nickel deposited on the truss. The thickness of the deposit, t , was calculated based on the theoretical density of Ni (8.9 g/cm^3) and the predicted surface area, S_A , of the truss determined from the CAD model (750.18 mm^2) using the following formula (units are mm and mg)

$$t = \frac{m_2 - \bar{m}_1}{\rho S_A} = \frac{m_2 - 66.2}{8.9(750.18)} \quad (1)$$

3.3.1.2. Direct: microscopic observation

For direct measurement a plated truss was first cast in epoxy under vacuum to ensure complete infiltration of the epoxy into the truss (Buehler EpoThin, Buehler, Lake Bluff, IL). The sample was then ground (300-1200 grit) and polished ($1 \mu\text{m}$ alumina) until the cross-section of the struts was exposed. Optical micrographs were then taken under 5-10x magnification. The thickness of the electrodeposited metal was measured at multiple points along the length of the struts from these micrographs using ImageJ (National Institute of Health, Bethesda, MD).

3.3.2. Grain Size

Average grain size was measured based on x-ray diffraction peak broadening. The x-ray diffraction pattern obtained from a sample of material deposited on the trusses was compared to the pattern obtained from a sample of conventional poly-Ni. Peak broadening was measured using MDI Jade 5

(Materials Data, Inc., Livermore, CA). The x-ray diffraction patterns were produced using Co-K α radiation with a wavelength of 17.9 Å.

3.4. Mechanical Testing

Mechanical testing was conducted on the as-received polymer template and on trusses with different thicknesses of electrodeposited nanocrystalline nickel. Samples were compressed at a loading rate of $2 \cdot 10^{-3}$ ϵ/s (180 $\mu\text{m}/\text{min}$ – strain calculated relative to entire height of the truss) in a Shimadzu Universal Testing Machine AG-50KNI (Kyoto, Japan) with a 50 kN load cell. Data were sampled at 10 Hz with a load resolution of 0.5 mN and a stroke resolution of 1 μm . Recorded displacements were adjusted for machine compliance based on the measured load. Compliance was measured without a sample present in the machine and was determined to be approximately linear ($1.48 \cdot 10^{-5}$ mm/N) over the relevant range of loads and displacements.

3.5. Electron Microscopy

Scanning electron microscopy (SEM) was used to observe the structure of the as-received rapid prototyped truss (Hitachi S-4500) and the plated truss (Hitachi S-2500). For the un-plated truss the sample was sputter coated with a thin layer of gold to provide the necessary electrical conductivity for the SEM to prevent charging of the sample. Samples were mounted to the aluminum sample holder with double sided conductive carbon tape. Additionally, a plated truss was analyzed in the SEM sequentially at three stages during a compression test: pre-yield (10% strain), immediately post-yield (17.5% strain) and far post-yield (25% strain) to understand the failure mechanisms. Note that these strains are calculated relative to entire height of the truss (1.5 mm) and not just the truss core height (0.98 mm).

4. Modeling

To accurately model the properties of the composite PCM it is first necessary to model the material properties of the constituent materials which make up the truss. For the polymer, a proprietary acrylic photopolymer (3D Systems Visijet HR), only an elastic modulus (1.724 GPa) and tensile strength (32 MPa) were provided by the manufacturer (Appendix A). Since no other data were provided it was assumed that the material is linearly elastic below the tensile strength and perfectly plastic above the tensile strength when loaded in compression, illustrated in Figure 24.

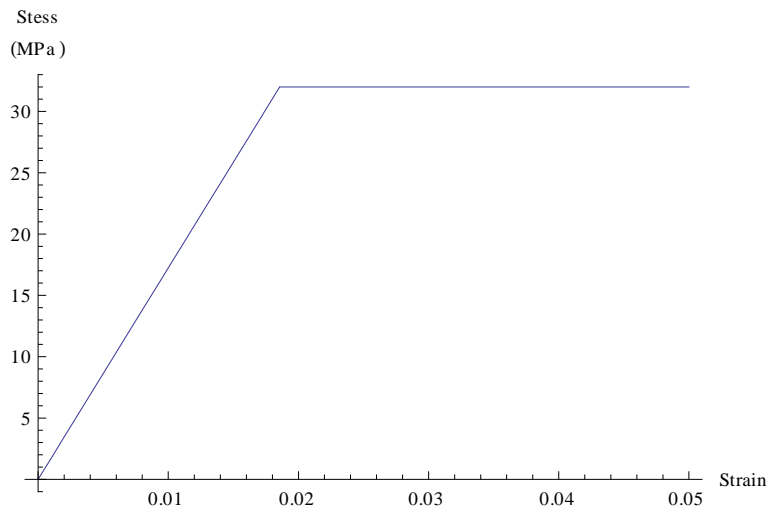


Figure 24: Assumed linearly elastic-perfectly plastic stress-strain plot for 3D Systems VisiJet HR

There are many possible ways to model the stress-strain curve for the electrodeposited nanocrystalline nickel. For this study the three-parameter Ramberg-Osgood model was selected as it has been used in previous studies on inelastic buckling and more specifically for applications concerning PCMs [40, 38, 41, 15, 6]. The Ramberg-Osgood equation for a 0.2% offset yield strength is given as

$$\epsilon = \frac{\sigma}{E} + 0.002 \left(\frac{\sigma}{\sigma_y} \right)^n \quad (2)$$

where ϵ is the true strain, σ is the true stress, σ_y is the yield strength (using a 0.002 offset), E is the elastic modulus and n is the hardening exponent. An experimental elastic modulus of 130 GPa was

determined by linear regression to the initial linear region of the true stress-true strain curve (Figure 25). By non-linear regression to the experimental tensile test data (Figure 25) a yield strength of 972.92 MPa and a hardening exponent of 10.191 was determined. The stress-strain curve was produced for a sample of nanocrystalline Ni. It was necessary to measure the grain size (using XRD) of the nickel electrodeposited on the trusses to confirm that it is nanocrystalline (grain size < 100 nm) and that the mechanical properties from the tensile test are representative of the Ni on the truss.

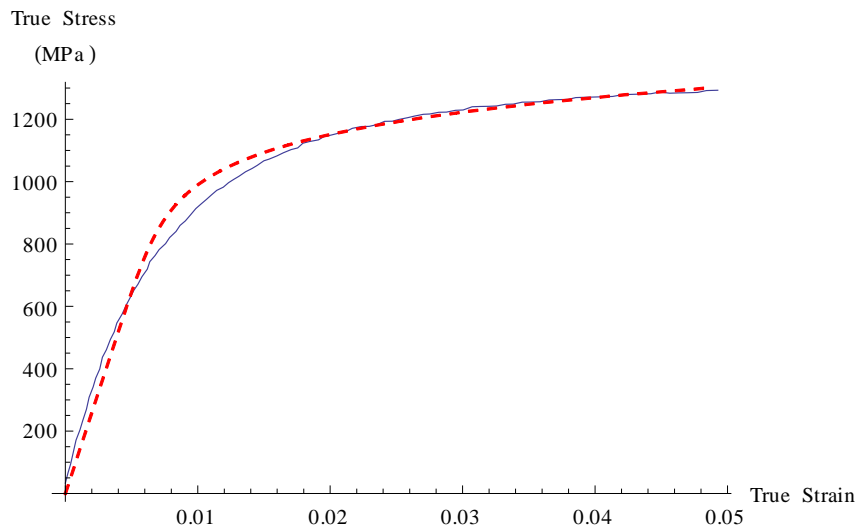


Figure 25: True stress - true strain curve from a tensile test of nano-Ni (solid line) and Ramberg-Osgood fit (dashed line)

The relevant material properties for the polymer and the nanocrystalline nickel are summarized in the following table (Table 2)

Table 2: Selected Material Properties

| Property | nano-Ni | 3D Systems Visijet HR |
|------------------------------|----------------------------|----------------------------|
| E | 130 GPa* | 1.724 GPa [28] |
| σ_y | 973 MPa | 32 MPa [28] |
| ν | 0.31 [42] | 0.41 [43] |
| n | 10.19 | ∞ |
| ρ | 8.9 g/cm ³ [42] | ~ 1 g/cm ³ [28] |

*The modulus reported for the electrodeposited nanocrystalline nickel is reduced compared to that of bulk polycrystalline Ni (207 GPa). Wei presented similar results showing reduced modulus in electrodeposited nanocrystalline nickel alloys [44]. Crystallographic texture has been proposed to cause the reduced modulus [44]

4.1. Analytical Model

4.1.1. Compressive Modulus

Assuming that all the compressive strain in the truss is transferred uniformly into the struts as pure axial tensile or compressive strain, using an energy balance the following relationship has been derived for a pyramidal lattice [45]

$$E = E_s V_f \sin^4 \theta \quad (3)$$

where E is the compressive elastic modulus of the truss, E_s is the elastic modulus of the individual struts, V_f is the solid volume fraction of the truss core (defined as the volume of all the struts in the truss core divided by the total volume of the truss core) and θ is the strut angle (45° -

Table 1). It is important to note that the majority of the literature uses the concept of relative density to describe the volume fraction. However, this concept becomes ambiguous when dealing with composite trusses composed of multiple materials (with different densities) and throughout this model the concept of volume fraction will be employed instead.

For the simple case of the as-received truss, the strut modulus, E_s , is equal to the tensile modulus of the polymer, 1.724 GPa. For the case of the composite Ni-polymer struts the strut cross-section was assumed to be composed of a rectangular polymer core (with idealized dimensions as defined by the CAD file,

Table 1) covered with a uniform thickness of Ni on all four sides (forming a larger rectangle offset from the core), illustrated below in Figure 26.

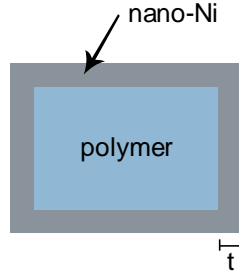


Figure 26: Composite strut cross-section, illustrating thickness (t) of nano-Ni plated on polymer core

Using the rule of mixtures assuming the strain in the polymer is the same in the nickel (for small strains) and that the interface between the deposited Ni and the polymer is perfect the following relationship was derived [42]

$$E_s = E_{Ni} \frac{A_{Ni}}{A_{tot}} + E_{poly} \frac{A_{poly}}{A_{tot}} \quad (4)$$

where E_{Ni} and E_{poly} are the elastic moduli for the nano-Ni (130 GPa) and the polymer (1.724 GPa), respectively, A_{Ni} and A_{poly} are the cross-sectional areas of the nickel and the polymer, respectively and A_{tot} is the total cross-sectional area of the strut. A_{poly} was calculated based on the dimensions from the CAD model to be 0.07 mm^2 (

Table 1). A_{tot} and A_{Ni} were both calculated as functions of the plating thickness, t (in μm), giving

$$A(t)_{tot} = (0.390 + t)(0.180 + t) \quad (5)$$

$$A(t)_{Ni} = A(t)_{tot} - A_{poly} = (0.390 + t)(0.180 + t) - 0.07 \quad (6)$$

Combining equations (4) through (6) gives the strut modulus as a function of plating thickness $E(t)_s$ and it can be seen that when $t = 0$, A_{Ni} is also 0 and equation (4) reduces to the simple case for the un-plated sample where $E_s = E_{poly}$.

The volume fraction (V_f) of the truss core was calculated by determining the total volume of struts in the truss core and then dividing this by the total volume of the core. The total volume of all the struts as a function of thickness is equal to the product of the strut length, the strut cross sectional area as a function of thickness ($A(t)_{tot}$) and the total number of struts (144). The total volume of the truss core was defined as the product of the base dimensions and the truss core height (the truss height without the facesheets)

$$V_f = \frac{V_{struts}}{V_{truss\ core}} = \frac{1.38 \times A(t)_{tot} \times 144}{310.5} \quad (7)$$

Combining equations (3) through (7) gives the modulus of the truss as a function of plating thickness, t , illustrated in the following plot (Figure 27). The calculated theoretical compressive modulus for the as-received truss ($t = 0$) was calculated to be 19.5 MPa.

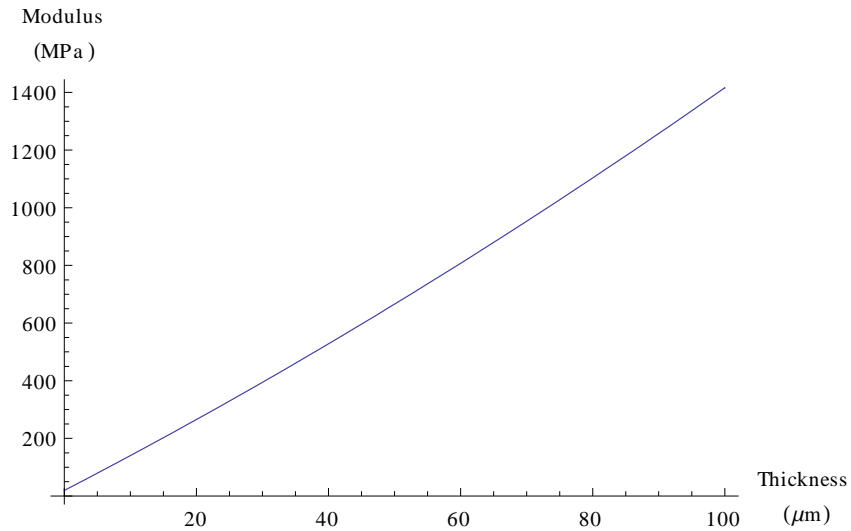


Figure 27: Plot of theoretical truss core modulus vs. thickness of electrodeposited nano-Ni

4.1.2. Peak Compressive Stress

A force balance in the z-direction (compression axis) has been used to derive an equation to relate the stress over the area of the entire truss (σ) to the average stress in the individual struts ($\bar{\sigma}_s$) [45]

$$\sigma = \bar{\sigma}_s V_f \sin^2 \theta \quad (8)$$

This relationship can predict the maximum stress in the entire truss if the maximum average stress in the individual struts which will cause buckling, yielding or fracture is known. If the struts are short and stocky they will fail either by yielding or by fracture, therefore

$$\bar{\sigma}_s = \sigma_y \quad (9)$$

where σ_y is the yield strength of the strut material (or the average failure stress over the strut area for a composite strut). Assuming that the load is transferred directly along the centroidal axis of the strut cross section and the struts are long and slender they will fail by elastic (Euler) buckling, where the critical Euler buckling force is given as [46]

$$\bar{P}_E = \frac{\pi^2 EI}{k^2 L^2} \quad (10)$$

where E is the elastic modulus of the strut material, k is a constant depending on the end fixity condition, L is the strut length and I is the moment of inertia for the section. The average stress over the strut is then given as

$$\bar{\sigma}_s = \frac{\bar{P}_E}{A_{tot}} = \frac{\pi^2 EI}{k^2 L^2 A_{tot}} \quad (11)$$

For the simple case of the as-received polymer truss the model does not account for any non-linear transition region between linear elasticity and perfect plasticity, this simplifies the analysis as the material will either fail by elastic buckling (long and slender struts) or by yielding (short and stocky struts) and not by a combination of both – known as inelastic buckling [47]. Therefore, to calculate the maximum stress it is only necessary to check if the theoretical Euler buckling stress for the strut exceeds the yield strength of the material. First the moment of inertia (I) for the section needs to be calculated. For the solid rectangular cross-section [47]

$$I_{poly} = \frac{bh^3}{12} = \frac{0.390 \times 0.180^3}{12} = 1.895 \times 10^{-4} \text{ mm}^4 \quad (12)$$

Substituting the values for the polymer elastic modulus (1.724 GPa), the moment of inertia (equation (12)), the strut length (1.38 mm), the end fixity condition constant ($\frac{1}{2}$ for fixed ends [47]) and the polymer strut cross sectional area (0.07 mm^2) into equation (11) gives $\bar{\sigma}_s = 96.07 \text{ MPa}$, which is much higher than the polymer yield strength of 32 MPa, therefore, the polymer strut should theoretically fail by yielding at 32 MPa and not by Euler buckling although imperfections in the strut can cause buckling at a lower load [46]. Combining equations (7) and (8) and substituting in the yield stress at which the strut was determined to fail at (32 MPa) gives the theoretical peak stress (σ) for the as-received polymer truss, 0.72 MPa.

As mentioned above when discussing the as-received truss, when the slenderness ratio of the strut lies in between the regions controlled either by yielding or purely elastic buckling the column will undergo inelastic buckling – a combination of local plastic deformation (hinging) and global structural instability [47]. This is the case for the struts plated with nano-Ni. Shanley [48, 49] developed a solution to this problem where the elastic modulus of the material is replaced in equation (10) with the tangent modulus for the material (E_t), defined as [47]

$$E_t = \frac{d\sigma}{d\epsilon} \quad (13)$$

The tangent modulus as a function of stress for the nano-Ni can be calculated by differentiating the Ramberg-Osgood equation (2) implicitly with respect to ϵ and solving for $\frac{d\sigma}{d\epsilon}$, giving

$$E_t = \frac{d\sigma}{d\epsilon} = \frac{500E\sigma}{500\sigma + En \left(\frac{\sigma}{\sigma_0}\right)^n} \quad (14)$$

Replacing E in equation (11) with E_t gives the critical inelastic buckling stress.

A common concept used to understand failure buckling failure is a column curve [38, 36]. A column curve illustrates the peak buckling stress as a function of a slenderness ratio, L/r_g , where r_g is the radius of gyration of the cross section and L is the length of the column. The radius of gyration

$$r_g = \sqrt{\frac{I}{A}} \quad (15)$$

where I is the moment of inertia for the column and A is the cross-sectional area of the column.

Rewriting equation (11) in terms of the slenderness ratio gives

$$\sigma_{crit} = \frac{\pi^2 E_t}{k^2 \left(\frac{L}{r_g}\right)^2} \quad (16)$$

The following column curve (Figure 28) represents the stress in the Ni as a function of slenderness ratio. The plot shows the inelastic buckling critical stress (based on the tangent modulus, E_t) as a solid line and the elastic buckling critical stress, where $E_t = E$, as a dashed line. The reader should note that the stresses in the Ni can exceed the yield strength of the material due to strain hardening during inelastic buckling.

The radius of gyration for the struts in the trusses was calculated by modeling the strut as a hollow rectangular tube – for this analysis the contribution from the polymer was ignored and the results are more important as an illustration of inelastic buckling and not for analytical predictions of truss mechanical properties since the critical stress is under-predicted as a result of ignoring the contribution of the polymer substrate to the peak stress.

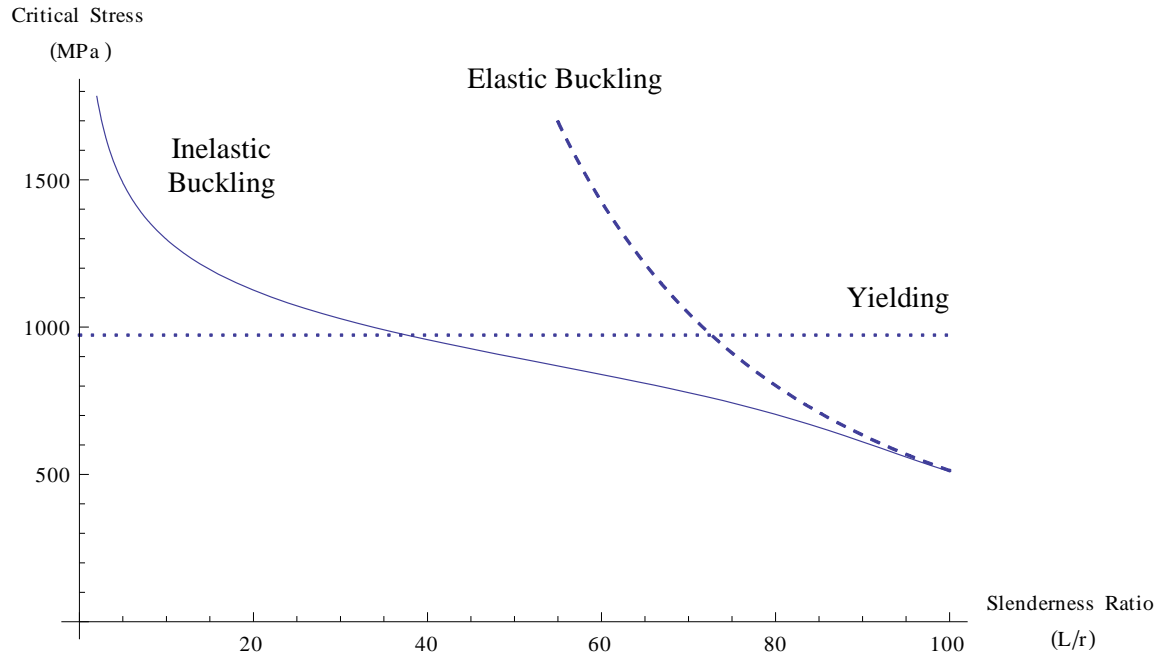


Figure 28: Column curve for nano-Ni, critical stress for elastic (dashed line), inelastic (solid line) buckling and yield (dotted line) vs. slenderness ratio. The peak stresses of the experimentally tested samples are plotted against their respective slenderness ratios and fall in the range of inelastic buckling.

Since the strut in the truss being analysed is not a single homogeneous material but actually a composite of two materials the column curve is not an accurate method to determine the critical stress. In addition, the nature of the interface between the Ni and polymer needs to be considered. Since the bond between the polymer and the nickel is not likely very strong a rule of mixtures approach cannot be used to calculate the average EI for the section. This assumption was verified during experimental testing as delamination of the nano-Ni from the polymer substrate was observed (Figure 37), suggesting that the interface is compromised during loading. This invalidates any isostrain assumptions inherent to the rule of mixtures. However, calculations revealed that for all thicknesses of electrodeposited nano-Ni the theoretical stress in the polymer exceeds the yield strength of the polymer. Based on the linearly elastic-perfect plasticity model of the polymer mechanical properties the polymer has effectively no stiffness beyond its yield strength. This assumption makes the contribution to the buckling stiffness (EI) of the strut from the polymer negligible; however, the polymer can still contribute to the load in the strut. EI for the strut is then given by

$$(EI)_{strut} = E_{Ni}I_{Ni} + E_{poly}I_{poly} = E_{Ni}I_{Ni} + 0 \quad (17)$$

where I_{Ni} is the moment of inertia for a hollow rectangular section with the same centroidal axis as the polymer section, given as a function of thickness in mm [47],

$$I(t)_{Ni} = \frac{b_2 h_2^3 - I_{poly}}{12} = \frac{(0.390 + t)(0.180 + t)^3}{12} - 1.895 \times 10^{-4} \text{ mm}^4 \quad (18)$$

The total force in the strut, P_s , is equal to the sum of the forces in the polymer and the nickel,

$$P_s = P_{Ni} + P_{poly} \quad (19)$$

From the forces it is possible calculate the stress over the strut area and in the constituent materials using the following relationship,

$$\sigma_i = \frac{P_i}{A_i} \quad (20)$$

Substituting equation (20) into equation (19) gives

$$\bar{\sigma}_s A_{tot} = \sigma_{Ni} A_{Ni} + \sigma_{poly} A_{poly} \quad (21)$$

Under the assumption that the polymer is post-yield and is perfectly plastic the stress in the polymer can be replaced with the polymer yield stress, 32 MPa and the area of the polymer can be replaced with the polymer strut area, 0.07 mm², giving

$$\bar{\sigma}_s A_{tot} = \sigma_{Ni} A_{Ni} + 32(0.07) = \sigma_{Ni} A_{Ni} + 2.24 \quad (22)$$

Substituting equation (22) into equation (11) gives (the assumption regarding the negligible contribution of the polymer to the overall EI of the strut has been included)

$$\bar{\sigma}_s A_{tot} = \sigma_{Ni} A_{Ni} + 2.24 = \frac{\pi^2 E_{Ni} I_{Ni}}{k^2 L^2 A_{tot}} \quad (23)$$

Replacing E_{Ni} in equation (23) with E_t from equation (14) gives the critical inelastic buckling stress. Note that k is again $\frac{1}{2}$ for fixed ends. This system of equations was solved for σ_s numerically by iterating the

stress in the nickel to find the tangent modulus and the critical inelastic buckling stress using Mathematica 6.0.1.0 (Wolfram Research, as before). The calculated theoretical peak stress is illustrated below in Figure 29 as a function of plating thickness.

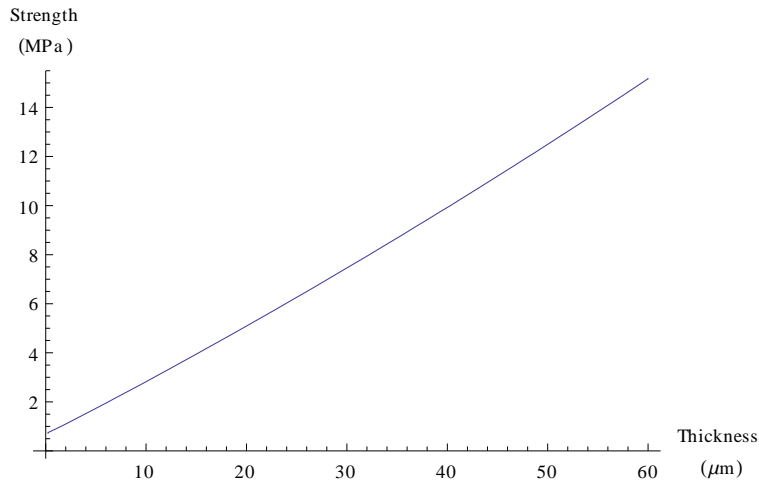


Figure 29: Theoretical peak stress over truss-area as a function of electrodeposited nano-Ni thickness.

The previous analysis relied on Euler beam theory. One of the assumptions in Euler's theory is that transverse shear forces are negligible and do not affect the maximum buckling force [46]. However, since the polymeric core is much softer in shear compared to the nano-Ni sleeve the effect of transverse shear on the buckling load should not be ignored [50, 47]. Various formulae have been developed to account for shear forces in the buckling of soft-core composite structures – the reader is referred to [50, 51, 52, 46] for additional information. An alternate model was developed based on the Engesser-type formula to account for the effect of transverse shear on the critical buckling load [51, 50]. This derivation is presented in Appendix B.

4.2. Finite Element Analysis

Finite element analysis has been widely and successfully used to predict the properties and understand the deformation of PCMs [53, 54, 55]. For this study two finite element models were created, one to measure the compressive modulus and the other to determine the peak compressive stress. The models

were constructed by directly meshing the CAD file geometry and then solving the models using the commercial finite element package ABAQUS 6.5 (Simulia, Dassault Systems, Suresnes, France).

The first model comprised the entire truss consisting of 122,057 linear tetrahedral elements (Figure 30). This analysis assumed only small displacements (linear analysis) and was used to determine the initial compressive elastic modulus of the truss. Unlike the analytical models which assume all the stress is carried by the struts, the finite element model is able to account for strain in the face-sheets, transverse expansion of the truss under compressive load and edge effects. Only the as-received polymer truss was modeled here using a linear elastic material model with the properties given in Table 2. The boundary conditions for the model included a small applied displacement in the negative z-direction (0.015mm, -1% strain relative to the total truss height) on the top surface while the bottom surface was prevented from rotating but transverse expansion was permitted – Poisson’s effect. To calculate the modulus the total reaction force from the top surface nodes was calculated and normalized by the projected area of the truss (316.84 mm^2), giving the applied stress. The strain was calculated as the applied displacement (0.015mm) divided by the height of the truss core (0.98mm) – analogous to the method used for the experimental data, giving the compressive strain. The modulus is then given by the applied stress divided by the strain in the truss core.

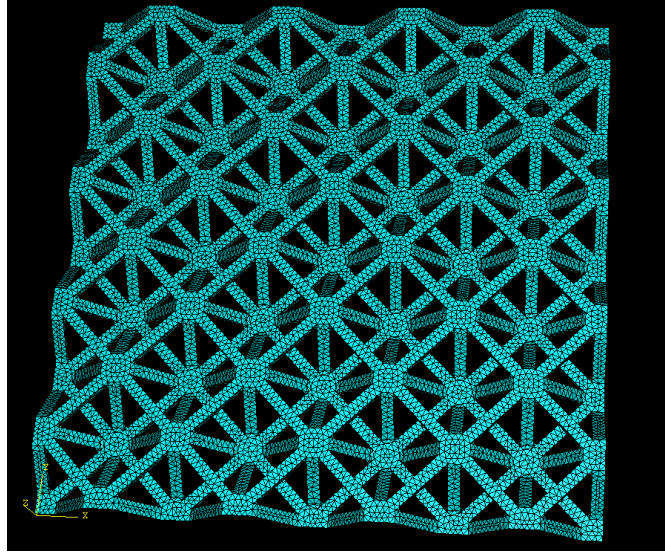


Figure 30: Discretized geometry of entire truss with 122,057 linear 4 noded tetrahedral finite elements.

Due to the high computational requirements of a non-linear analysis the second model consisted of only a single unit-cell with four struts and periodic boundary conditions to simulate an infinite sheet of repeated unit cells. The model consisted of 71,269 linear tetrahedral finite elements (Figure 31). This model was non-linear and solved for large displacements (>30% strain). The boundary conditions were similar to the linear analysis, with an applied displacement to the top surface in the negative z-direction of 0.3mm, except for this model all boundaries along the edges of the unit-cell were fixed to prevent transverse expansion (equivalent to modeling an infinite plane of unit cells). For this model the polymer mechanical properties were described using the ABAQUS deformation plasticity theory using the previously assumed linearly elastic behavior up to the yield stress followed by perfect plasticity. The resulting model was solved iteratively. The reaction forces from the top surface were summed at each time step and the maximum resulting sum represents the peak compressive load before collapse. This value was converted into a full-truss-equivalent stress by multiplying the value by the number of unit-cells in the full truss (36 – note that nodes on the edge have three struts and are considered to be $\frac{3}{4}$ of a full node which has four struts) and then divided by the projected area 316.84 mm^2 .

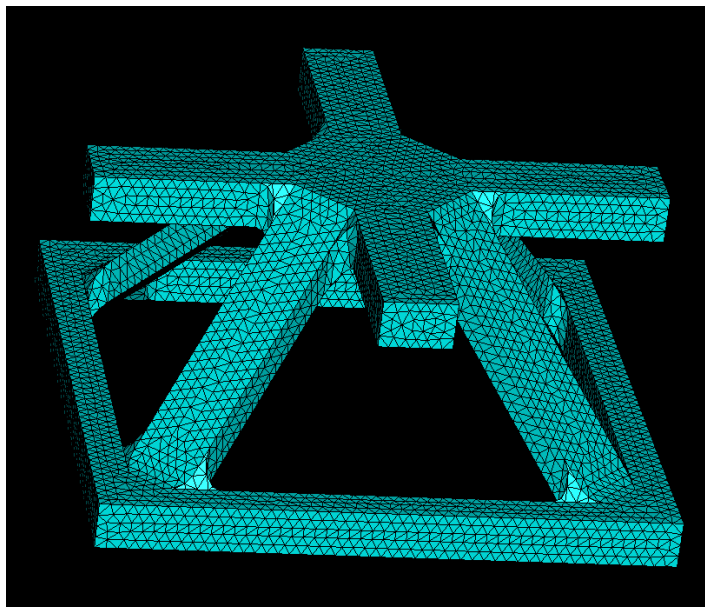


Figure 31: Non-linear finite element model of single unit cell. Mesh consists of 71,269 linear 4 noded tetrahedral elements.

5. Results and Discussion

5.1. Coating Properties

5.1.1. Thickness

Measured masses of the 12 samples tested ranged from 66.2 mg (as received) to 371.3 mg. This correlated to a range in plating thicknesses from 0 μm to 45.69 μm .

Measurement of plating thickness from optical micrographs of a ground and polished sample with a calculated thickness of 45.1 μm found that plating thicknesses on the struts at the edge of the truss ranged from approximately 30 μm to 70 μm . Greater variability in substrate thickness and plating thickness was found on the underside of the truss due to substrate contact with the support material during rapid prototyping. The variation in surface topography from the top to the bottom can also be seen in the electron micrographs of the as-received polymer truss. Figure 32 shows a representative optical micrograph of a polished strut cross-section.

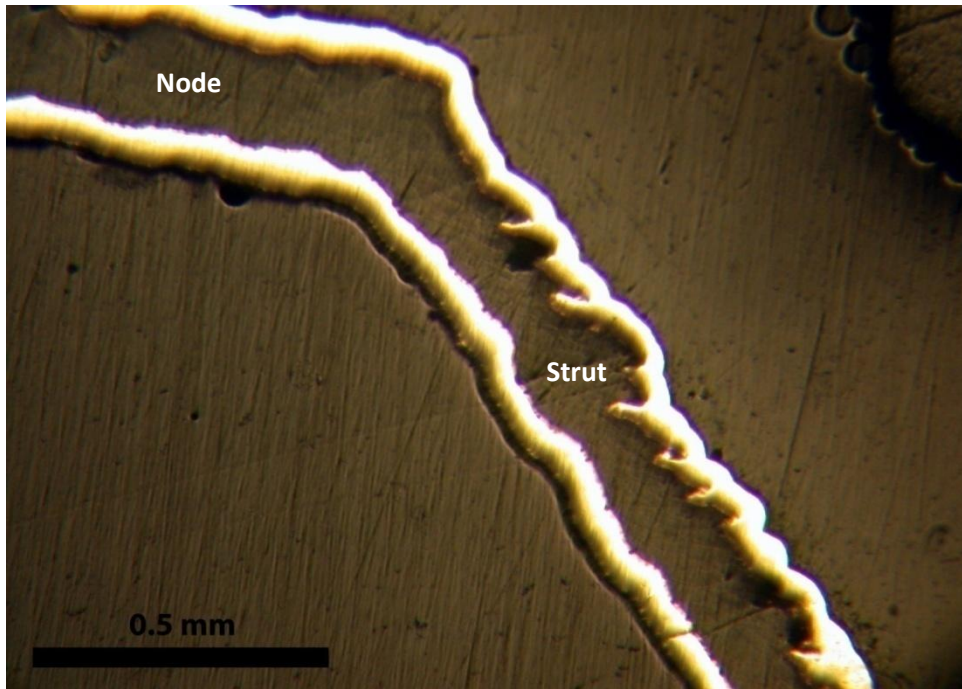


Figure 32: Representative optical micrograph of a ground and polished strut cross-section illustrating substrate and plating thickness variability. The thickness can be seen to vary more on the underside of the truss (shown on the top in this figure) due to contact with the support material during the rapid prototyping process. Node and strut section labeled on the cross-section

5.1.2. Grain Size

Average grain size was found to be 21.5 nm based on x-ray diffraction peak broadening. Measured using MDI Jade 5 (Materials Data, Inc., Livermore, CA). The x-ray diffraction peaks are presented in Figure 33.

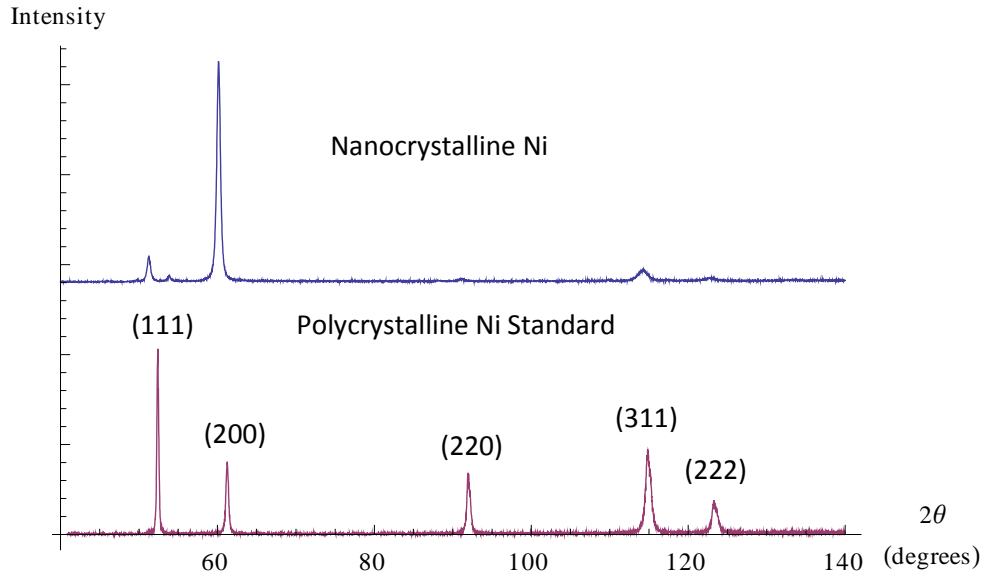


Figure 33: X-ray diffraction patterns for polycrystalline Ni standard (lower) and nanocrystalline Ni (upper). Peak broadening due to reduced grain size is apparent. Differences in relative peak intensity indicate the crystallographic texture of the sample. (Co-K α radiation $\lambda = 1.79 \text{ \AA}$).

5.2. Electron Microscopy

Scanning electron microscopy of the as received polymer truss revealed the rough surface texture on the underside of the truss due to the contact between the polymer and the support material during the rapid prototyping. The rough stippled surface texture can be seen in Figure 34. The upper surface which is not in contact with the support material is substantially smoother.

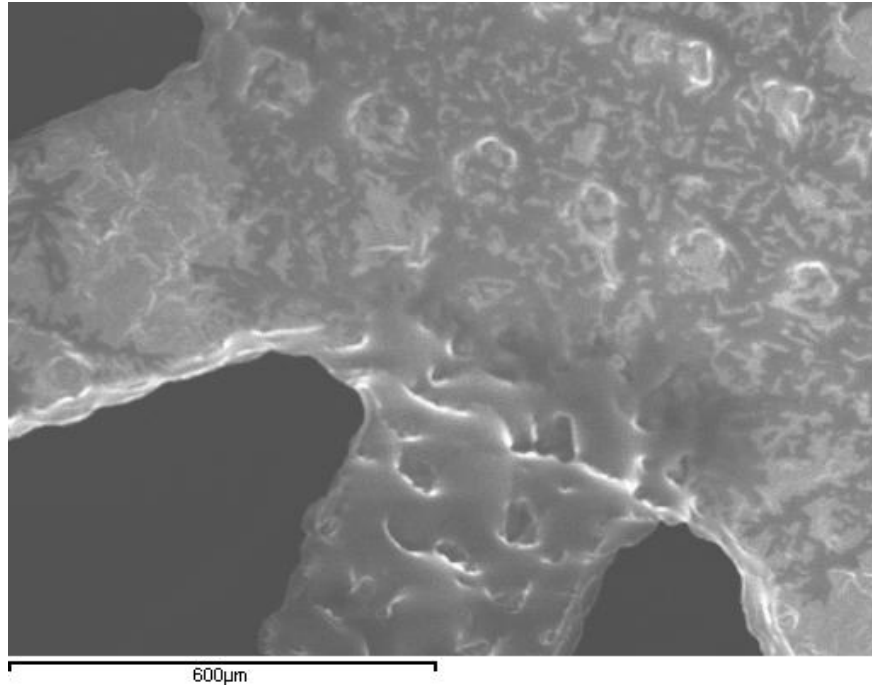


Figure 34: Scanning electron micrograph of rough lower surface of as-received polymer truss.

Following electrodeposition it was seen that the electrodeposited nickel conforms to the smooth surface texture present on the top of the truss, this can be seen in Figure 35a. Comparing Figure 35a to Figure 35b, which illustrates the rough surface of the nickel on the underside of the truss the difference, is clear.

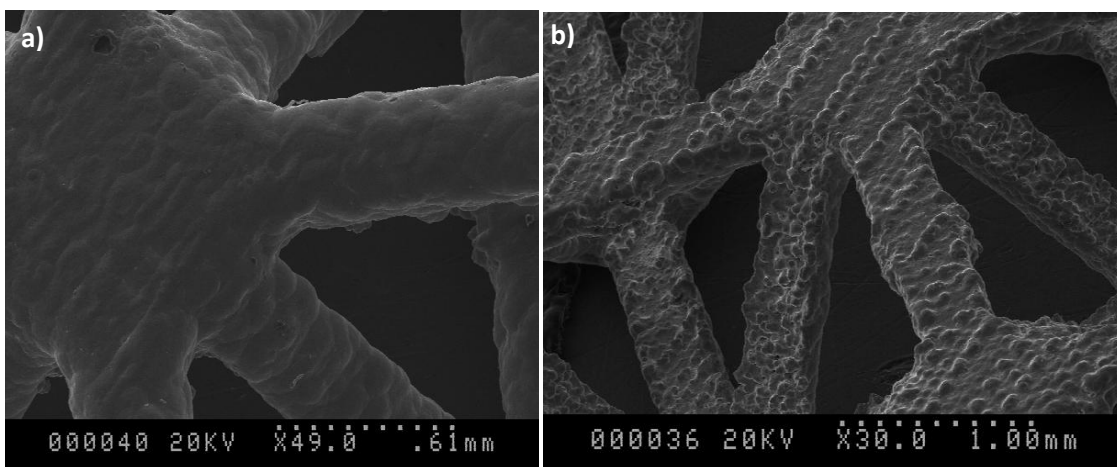


Figure 35: Scanning electron micrographs of the upper (a) and lower (b) surfaces of electrodeposited nickel on the truss illustrating the smooth (a) and rough (b) textures produced due to substrate roughness.

During a compression test the sample was removed from the mechanical testing machine at three points during the test: pre-peak, immediately post-peak and far post peak to view the sample in the SEM. Pre-peak imaging at 10% strain revealed no damage or cracking occurring before the peak load. Imaging immediately after the peak stress, at 17.5% strain, failure was evident in the corner diagonal struts of the face-sheets and it is clear that for the plated trusses the max load is reduced due to the failure of the face-sheets before the struts. Figure 36 illustrates the cracking which was discovered upon examination of the truss in the SEM after compression to just over the peak stress.

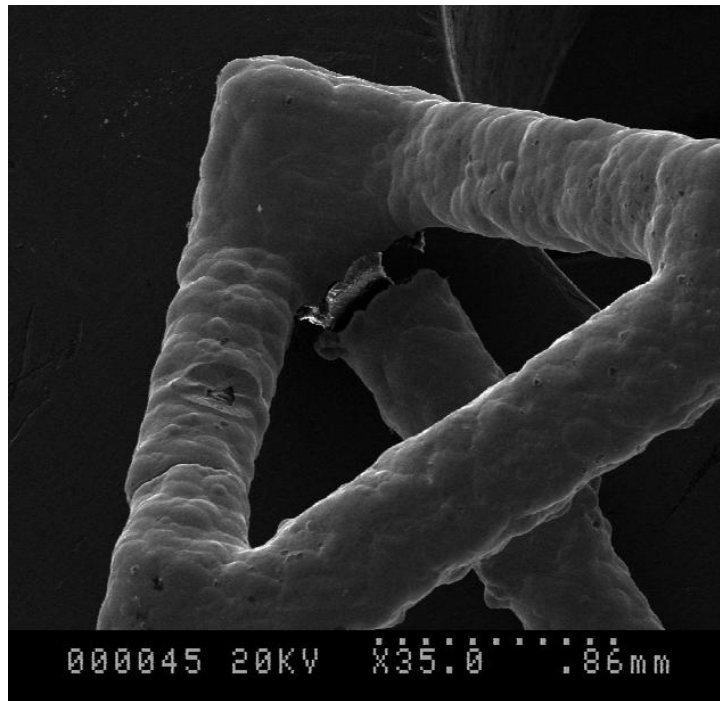


Figure 36: SEM micrograph illustrating cracking which occurred in the diagonal corner struts of the face-sheet immediately after the peak load.

The sample was then compressed further to 25% strain, during this period the load continued to drop due to buckling of the struts. Scanning electron microscopy of the truss after extensive compression revealed that additional struts in the face-sheet had failed and that the majority of the struts had buckled. The buckling of the struts produced a localized wrinkling and delamination of the nano-Ni electrodeposit from the polymer substrate. This confirms the supposition that the bond between the Ni

and the polymer is not strong enough to support extensive load transfer. Figure 37a shows one of the additional struts in the face-sheets which had failed after continued loading and Figure 37b is a higher magnification view of the fracture surface. In the higher magnification view it can be seen that during failure of the strut the nano-Ni delaminates from the polymer substrate. Figure 38a illustrates the buckling of the struts and highlights the areas of wrinkling in the nickel electrodeposit due to inelastic buckling. Figure 38b shows a higher magnification micrograph of a single strut; the global buckling and the localized wrinkling of the nano-Ni layer are easily observed. Figure 39 shows the difference in straightness between a strut which has buckled and one which remains intact, it can be seen that the buckling of the strut remains after the load is taking off which indicates permanent plastic deformation has occurred – characteristic of inelastic buckling [46].

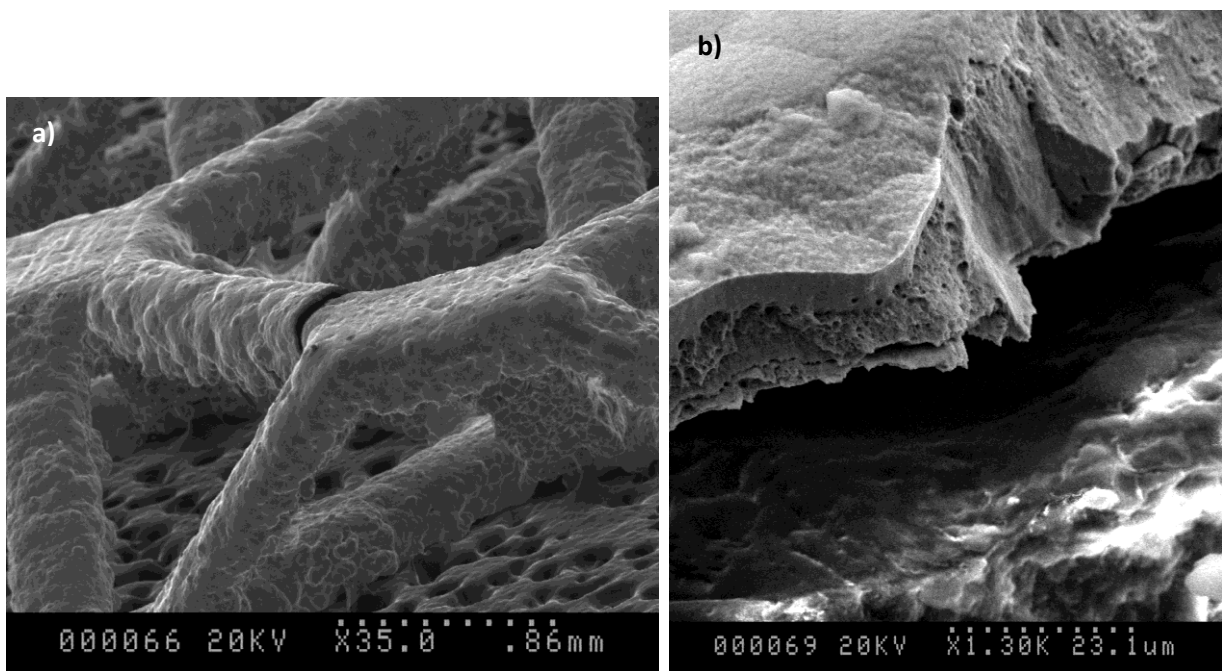


Figure 37: (a) Scanning electron micrograph of sample after extensive compression showing the failure of an additional strut in the face-sheets and (b) magnified section of fracture surface of the failed face-sheet strut, the delamination of the nano-Ni from the polymer substrate is clearly evident, note the charging of the non-conductive polymer surface.

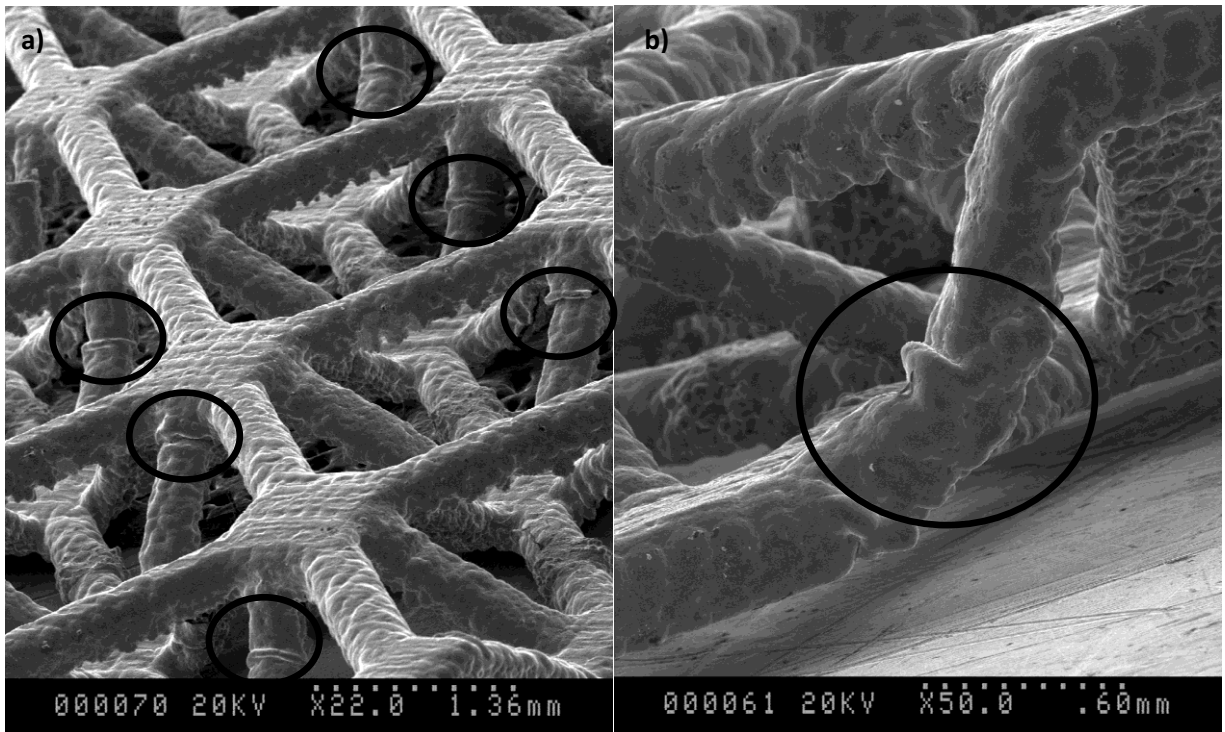


Figure 38: (a) SEM micrograph showing the extensive buckling of the struts after continued deformation. (b) Individual buckled strut. The wrinkling in the strut is immediately evident as is the fact that the strut is no longer straight. Regions of local wrinkling and delamination are circled.

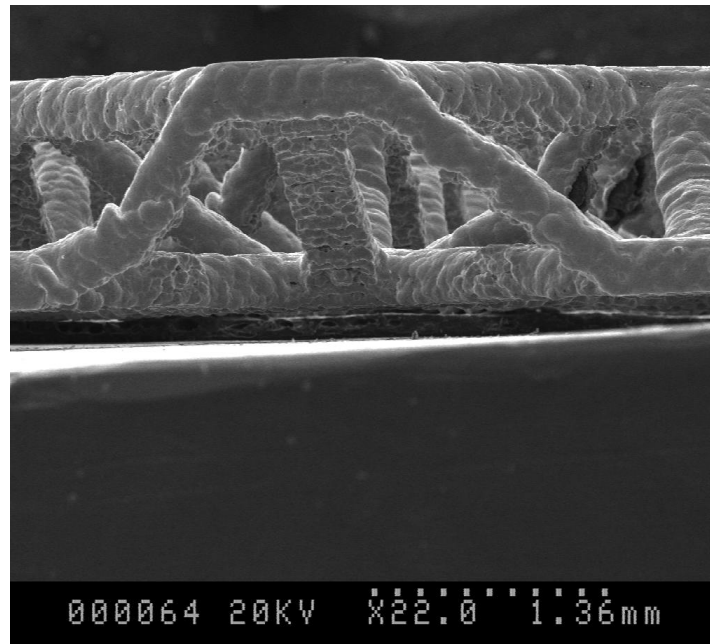


Figure 39: Micrograph which illustrates the global buckling of the strut on the left compared to the strut on the right which is still straight.

5.3. Compression Tests

Figure 40 shows the stress-strain curve for compression testing of the as-received polymer truss. Figure 41 shows a representative full stress-strain curve for a sample with a 45 μm thick nano-Ni layer. The stress-strain curve is characterized by five regions, the initial linear elastic region, the peak stress, the post-peak softening, the small plateau region and the final densification. Figure 42 illustrates the initial portion of five stress-strain curves for different thickness of nano-Ni plating on the polymer substrate. It can be qualitatively seen that with increasing thickness the stiffness and the peak stress both increase, however, there is little effect on the densification strain. By comparing the stress strain curves for the plated trusses and the as-received polymer trusses not only is the strength and stiffness much higher but the relative level of the plateau stress is much lower in the polymer truss than the plated trusses. The stress strain curve for the polymer truss exhibits a very low plateau stress as the struts fracture during compression. The increased plateau stress of the plated trusses is due to the ductility of the nano-Ni compared to the relatively brittle polymer, the nano-Ni can continue to deform under continued compression and carry some load while the individual polymer struts fracture and no longer contribute to the load carrying ability of the truss.

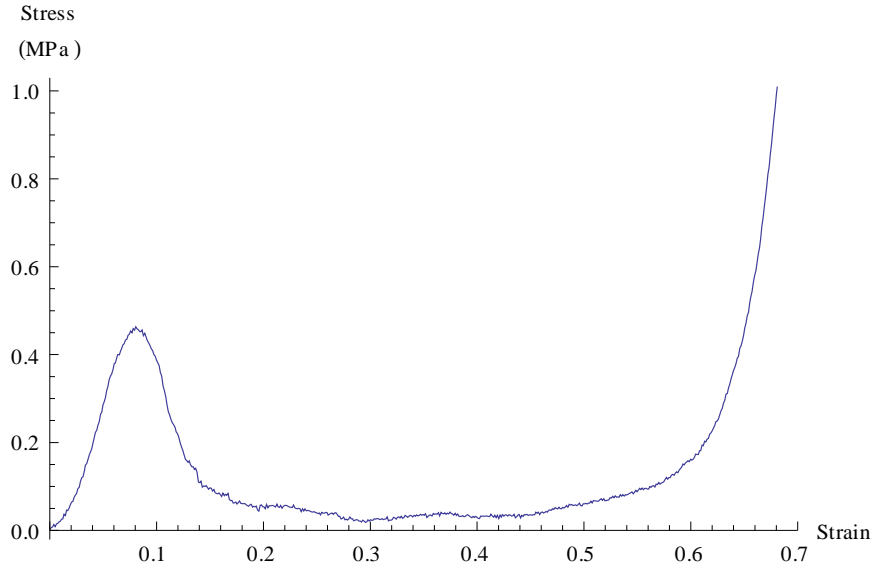


Figure 40: Stress-strain curve for compression test of as-received polymer truss. Note the very low stress level over the plateau due to minimal ductility of the polymer. Displacements have been adjusted for machine compliance and strains are relative to entire truss height, 1.5mm.

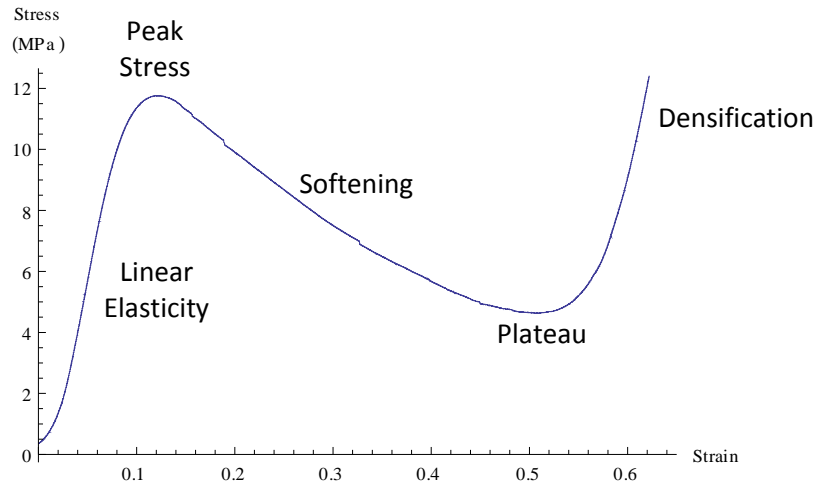


Figure 41: Full stress-strain curve for 45 μm thick nano-Ni plating sample. The five regions which make up the stress-curve are labeled on the curve the initial elastic linear region, the peak stress, the post-peak softening, the small plateau region and the densification region. Displacements have been adjusted for machine compliance and strains are relative to entire truss height, 1.5mm.

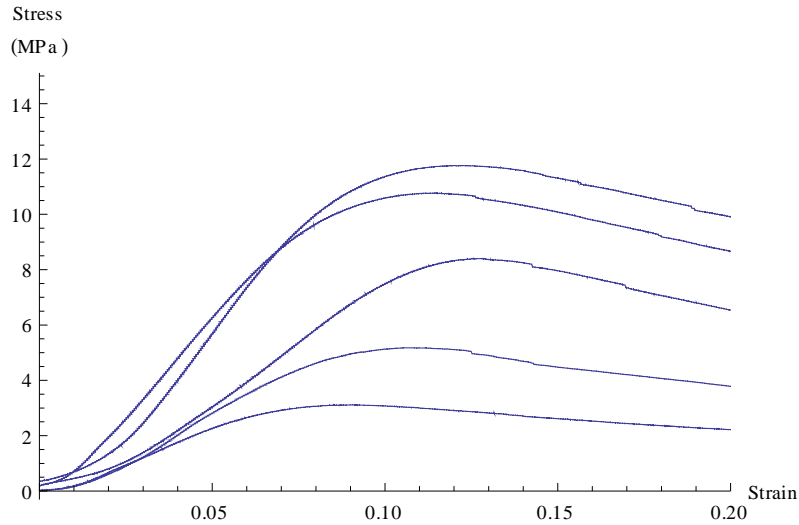


Figure 42: Sample stress-strain curves from compression testing of 5 trusses with increasing thicknesses of nano-Ni plating: 15, 26, 33, 40 and 45 μm . Increasing modulus and strength with increasing nano-Ni thickness is apparent. Displacements have been adjusted for machine compliance and strains are relative to entire truss height, 1.5mm.

Closer examination of the stress-strain curves for the plated samples reveals a series of nearly instantaneous drops in load occurring after the peak load (Figure 43a). These small load drops can be seen more clearly by plotting the tangent to the stress-strain curve as a function of strain, illustrated in Figure 43b, as per [33]. The series of drops in load appear as large negative spikes in the slope of the tangent within a region of otherwise nearly constant slope. These small drops in load are attributed to the failure of the nano-Ni sleeves surrounding the facesheet struts and the delamination of some of the nano-Ni from the polymer substrate in the face-sheet after the peak load. These failures were observed using scanning electron microscopy of a truss sample removed from the compression test just after the peak load (Figure 36 and Figure 37).

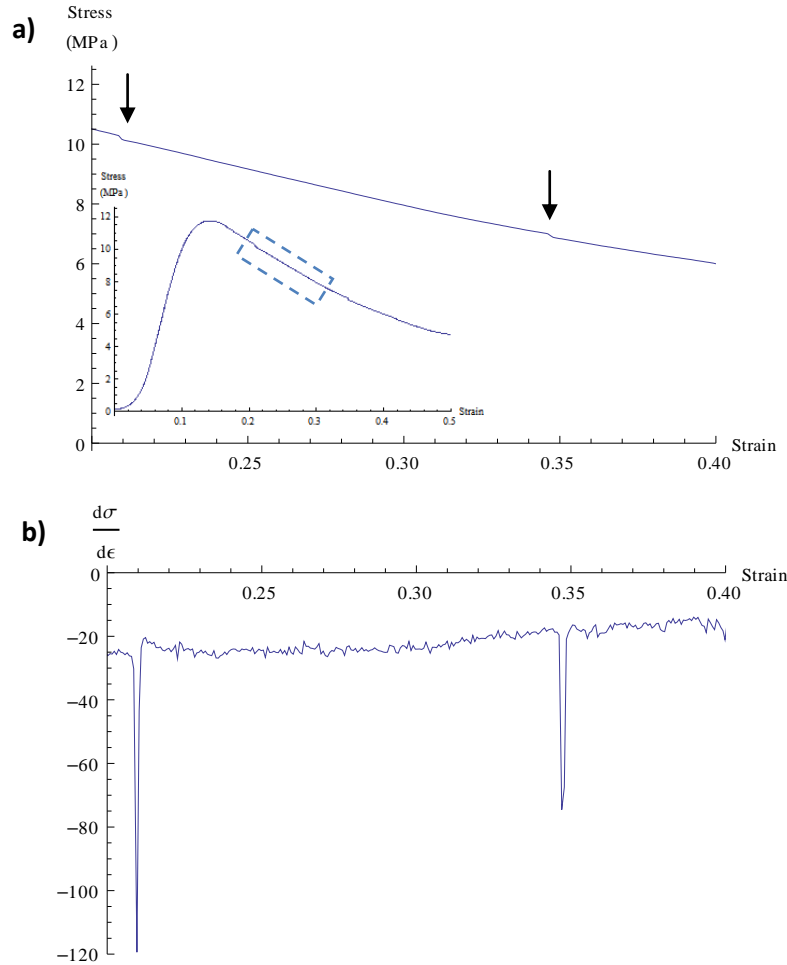


Figure 43: (a) Failure occurring in the nano-Ni sleeves characterized by a series of nearly instantaneous load drops (indicated with arrows) visible in the post-peak region of the stress-strain curve. The inset figure highlights the region of interest plotted in the larger figure. (b) shows slope of tangent to stress strain curve – rapid decreases correlate with the load drops visible in (a). Sample has a plating thickness of 45 μm . Displacements have been adjusted for machine compliance and strains are relative to entire truss height, 1.5mm.

Similar cracking is not evident before the peak stress occurs. This indicates that irreversible damage is not occurring before the initial cracking which begins just after the peak stress. Figure 44 illustrates the slope of the tangent for all strains from the start of the test to the plateau region and it can be seen that no large spikes are visible on the curve before the peak strength. The peak strength is located at the first zero-crossing of the curve representing a horizontal tangent characteristic of a local maxima.

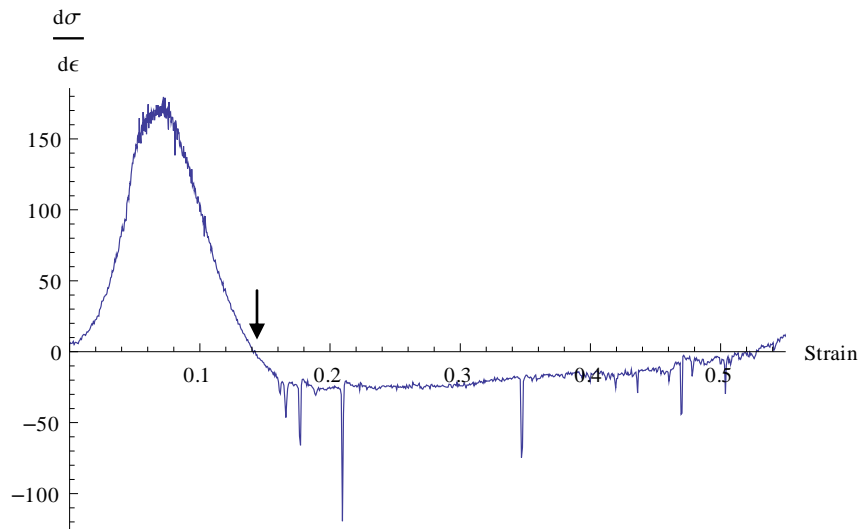


Figure 44: Slope of tangent to stress-strain curve as a function of strain from start of compression test to plateau region. Peak stress located at the first zero-crossing of the curve at a strain of approximately 14% (indicated with the arrow). The second zero-crossing indicates the plateau strain.

5.4. Compressive Modulus

As shown in the stress-strain curves (Figure 40 and Figure 42) the truss samples exhibited linear elastic behavior before buckling instability occurred. The compressive modulus was determined from the slope of a linear regression to the linear portion of the stress-strain curve. Bouwhuis and Hibbard found that during loading of truss cores initial bedding-in effects can lead to a reduced modulus and the compressive modulus should be measured from the slope of an unloading/reloading curve during within the linear elastic region [56]. Testing of the trusses for this study found that the loading and unloading curves overlap, similar to the results presented by Wallach and Gibson [57]. The lack of bedding in effects is attributed here to the face sheets which are an integral part of the truss samples unlike the truss cores tested by Bouwhuis and Hibbard [56]. Table 3 summarizes the predicted and measured compressive modulus for each of the samples.

Table 3: Predicted and measured compressive modulus for mesoscale truss structures along with nano-Ni coating thickness. The measured modulus is also expressed as a % of the theoretical value.

| Sample | Plating Thickness (μm) | Compressive Modulus (MPa) | | % of Theoretical |
|-----------|-------------------------------------|---------------------------|----------|------------------|
| | | Predicted | Measured | |
| 1 | 0.00 | 19.40 | 5.6 | 28.8 |
| 2 | 26.13 | 344.1 | 48.6 | 14.1 |
| 3 | 33.37 | 439.1 | 105.8 | 24.1 |
| 4 | 27.69 | 364.3 | 46.3 | 12.7 |
| 5 | 32.62 | 429.2 | 62.0 | 14.4 |
| 6 | 41.26 | 545.1 | 94.1 | 17.3 |
| 7 | 44.40 | 588.1 | 104.7 | 17.8 |
| 8 | 45.69 | 605.8 | 100.2 | 16.5 |
| 9 | 14.66 | 198.1 | 31.3 | 15.9 |
| 10 | 15.33 | 206.4 | 35.3 | 17.1 |
| 11 | 14.50 | 196.8 | 30.0 | 15.2 |
| 12 | 15.60 | 209.9 | 33.0 | 15.8 |

The data from Table 3 is illustrated in Figure 45 – showing the measured modulus as a function of plating thickness for all the samples along with the predicted modulus as function of thickness. From the figure it can be seen that the predicted modulus consistently exceeds the measured modulus for all the samples. Similar over predictions of the compressive modulus have been published in similar studies [36, 45, 58, 13]. The model used to predict the compressive modulus assumes that all strain energy is transferred into the struts as purely axial deformation [45]. The model does not account for reduction in modulus caused by edge effects, additional modes of deformation (ex. bending) caused by defects in the structure, strain absorbed by the face sheets or transverse expansion of the truss. Preventing transverse expansion by confining the truss laterally during compression (or producing a truss with rigid face-sheets) has been shown to reduce transverse expansion and increase the measured compressive modulus [56, 13]. It is also possible that the constituent material properties used in the analysis which were measured in tension differ from the actual compressive properties of the materials. Although for traditional materials the tensile and compressive properties are usually the same for many polymers and nanocrystalline metals this is not the case [59, 60].

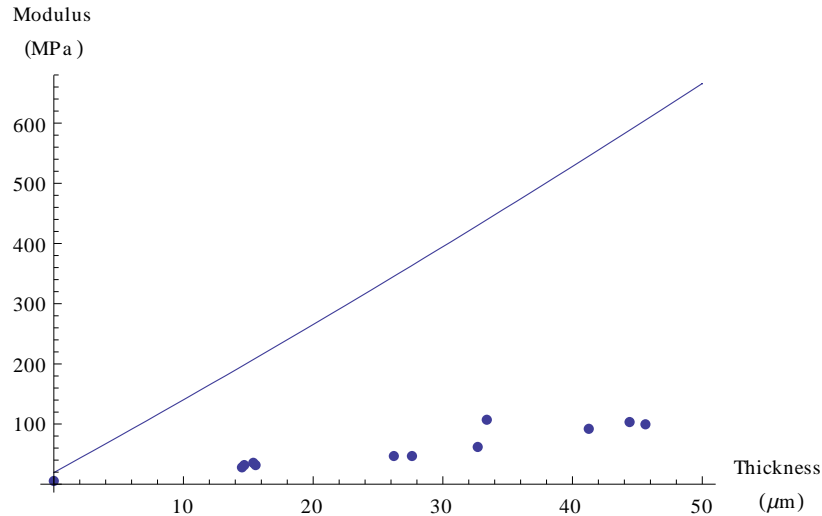


Figure 45: Plot of measured modulus (points) along with theoretical prediction (solid line)

5.4.1. Finite Element Prediction

By applying a small displacement of -0.015 mm in the z-direction to the top surface of the model of the entire truss and calculating the sum of the reaction forces of the top nodes the total force was calculated. The force was found to be 62.28 N. Dividing the force by the projected area of the truss (316.84 mm^2) gives a stress of 0.197 MPa. To calculate the strain in the truss core the applied displacement is divided by the truss core height, 0.98mm, giving a strain of 1.53%. The linear compressive modulus is then calculated by dividing the stress by the strain, $0.197/0.0153 = 12.87$ MPa. Comparing this value for the compressive modulus to the experimentally measured value for the as received polymer truss, 5.6 MPa it can be seen that this value is much closer than the value calculated by the analytical model of 19.4 MPa. The finite element model accounts for edge effects and transverse expansion of the truss which explains the improved prediction; however, there is still a fairly significant error between the theoretical prediction and the experimentally measured value. The experimental value is likely lower than the theoretical due to small geometrical imperfections produced during rapid prototyping. Figure 46 illustrates the von Mises stress in the truss calculated following the applied displacement to the top surface.

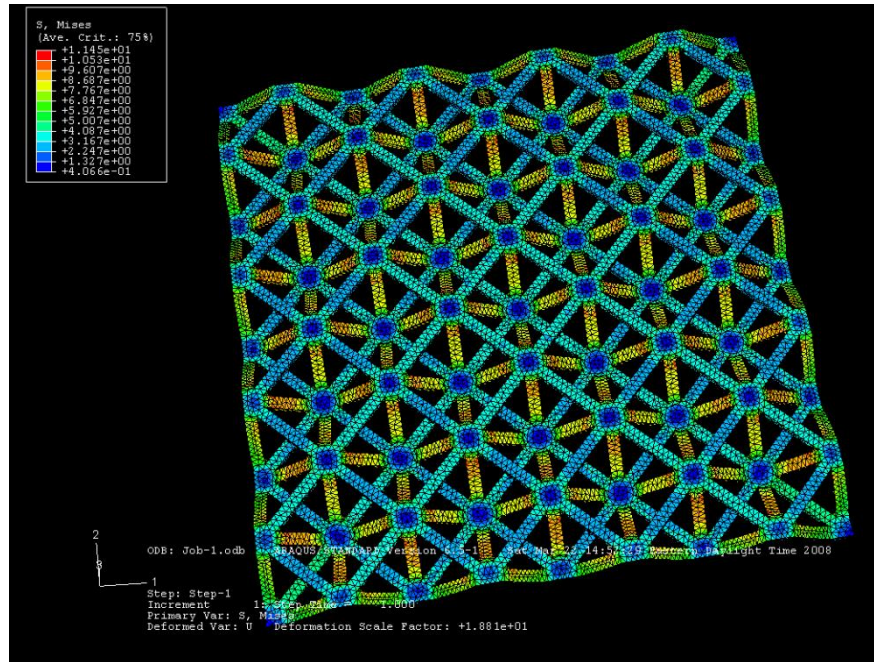


Figure 46: von Mises stress in full truss model (linear) after application of 0.015mm compressive displacement in the z-axis. Maximum stress of 11.4 MPa, deformation exaggerated by a factor of 18.8x.

5.5. Peak Compressive Strength

Using the constituent properties of the constituent materials and the analytical model developed the peak compressive stress for the as-received un-plated truss and the plated trusses were calculated.

For the case of the as-received truss the predicted peak strength based on the polymer yield strength was 0.7 MPa and the measured peak strength was 0.49 MPa. This discrepancy is likely the result of defects produced during the rapid prototyping process and an unrealistic and oversimplified model of the polymer's compressive properties.

Upon examination of the SEM micrographs of the surface of the as-received truss (Figure 34) the rough surface texture is immediately evident. These surface imperfections act as defects which reduce the critical buckling stress. In addition, geometrical inaccuracy due to the rapid prototyping process can further reduce the critical buckling stress.

For many materials a tensile test is adequate to determine the compressive strength, however, for the case of polymeric materials there can be significant differences between the compressive and tensile properties [59]. For this study only the tensile properties of the rapid prototyping polymer were available. Differences between the reported tensile properties (Appendix A) and the compressive properties would have an effect on the predicted peak stress. Running a compression test on a suitable sample of the polymer would provide much for useful data from which to model the buckling behavior of the polymeric struts. Furthermore, the linearly elastic and perfectly plastic model (Figure 24) used to describe the behavior of the polymer is most probably not representative of the true (most certainly non-linear) post-yield behavior of the polymer. During evaluation of the polymer truss following mechanical testing it was found that the struts appear to have fractured in a brittle manner. This fracture could have occurred at a stress below the predicted yield stress due to stress concentrations. This could account for the reduced maximum stress.

Various thickness of nanocrystalline nickel was deposited on the rapid prototyped trusses (14.56 μm to 45.69 μm) Using the analytical model developed and the thickness of the electrodeposited nano-Ni the peak strength of each truss was calculated. Table 4 lists the predicted peak stress and the experimentally measured peak stress along with the thickness of nano-Ni for each of the 12 samples tested.

Table 4: Predicted and measured peak strength for mesoscale truss structures along with nano-Ni coating thickness

| Sample | Plating Thickness (μm) | Peak Compressive Stress (MPa) | | % of Theoretical |
|--------|-------------------------------------|-------------------------------|----------|------------------|
| | | Predicted | Measured | |
| 1 | 0.00 | 0.72 | 0.49 | 68.1 |
| 2 | 26.13 | 6.53 | 5.18 | 79.3 |
| 3 | 33.37 | 8.28 | 8.30 | 100.3 |
| 4 | 27.69 | 6.90 | 6.49 | 94.0 |
| 5 | 32.62 | 8.09 | 8.40 | 103.8 |
| 6 | 41.26 | 10.24 | 10.76 | 105.0 |
| 7 | 44.40 | 11.05 | 11.76 | 106.5 |
| 8 | 45.69 | 11.38 | 11.70 | 102.8 |
| 9 | 14.66 | 3.87 | 2.80 | 72.4 |
| 10 | 15.33 | 4.02 | 2.87 | 71.4 |
| 11 | 14.50 | 3.85 | 2.67 | 69.4 |
| 12 | 15.60 | 4.08 | 3.10 | 76.0 |

The data from Table 4 is illustrated in Figure 47 – showing the peak stress as a function of thickness for all the samples along with the predicted peak stress as function of thickness. From the figure it can be seen that the predicted peak stress overestimates the peak stress for the lower plating thicknesses and slightly underestimates the peak stress for the higher plating thickness plated samples.

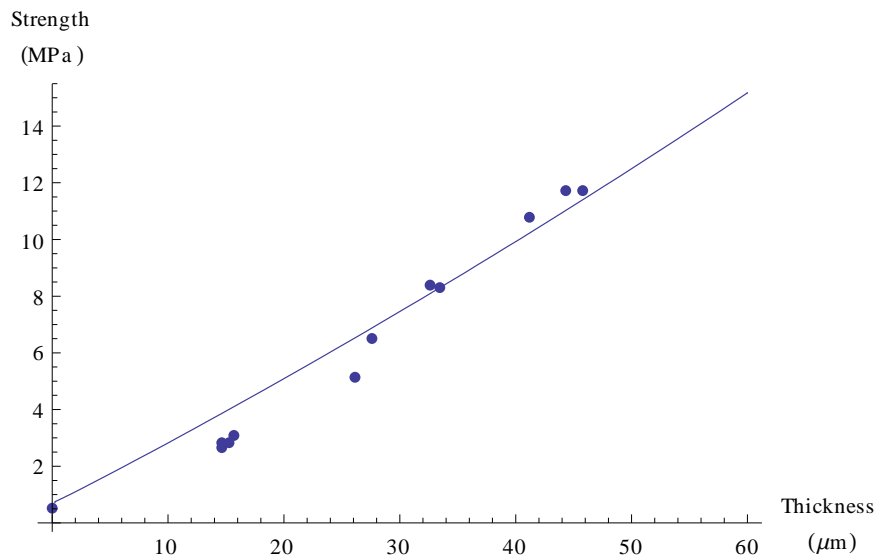


Figure 47: Measured peak compressive stress (points) and theoretical peak compressive stress (solid line) as a function of plating thickness

The previous plot (Figure 47) which illustrates the measured peak compressive stress along with the theoretical peak compressive strength both as functions of plating thickness provides a clearer understanding of the nearly linear relationship between peak compressive stress and plating thickness.

Figure 47 illustrates the difference between the predicted theoretical peak compressive stress and the experimentally measured peak stress. The reduction in strength compared to the theoretical maximum value at lower thickness is attributed to non-uniform buckling of the struts and defects in the structure [36]. The defects which likely contribute to the reduced strength are easily seen in the SEM micrographs of the surface of the nano-Ni plating (Figure 35). Similar to the case of the polymeric truss it is likely that the material properties measured in tension for the nano-Ni are not exactly the same as the compressive properties of the material. Although for most metals there is symmetry between tensile and compressive properties an asymmetry has been observed in many nanocrystalline metals [60]. Although difficult, direct compression testing of an individual strut could be used to better determine the actual compressive properties of the nano-Ni. This tension-compression asymmetry could cause either the over or under prediction. Reduced critical buckling stress compared to the theoretically predicted maximum values has been found to be caused by residual stresses in the column due to certain fabrication process such as cold rolling of steel [47]. During electrodeposition residual stresses have been found to form in the deposit and similar to steel columns, these stresses could act to reduce the critical buckling stress [61]. The most likely reason for the under prediction of peak stress at higher thickness is that the model assumes that all the stress is carried by the struts in the truss core and no stress is contained within the nodes or the face-sheet, this assumption is likely not valid across the range of thickness. Reducing the magnitude of the error due to the face-sheets could be done testing a much larger multi-layered truss.

5.5.1. Finite Element Prediction

By applying a large displacement of -0.3 mm in the z-direction to the top surface of the finite element model of a single unit cell and calculating the sum of the reaction forces of the top nodes at each time step a stress-strain curve can be created from the finite element analysis. The force was multiplied by the total number of unit cells in the truss (36) and then divided by the projected area of the truss (316.84 mm^2) to determine the full-truss-equivalent stress. The displacement was divided by the height of the truss core (0.98 mm) to determine the strain in the truss core. Figure 48 shows the stress-strain profile from the finite element analysis, the reaction force is only evaluated once each time step so to ensure that rapid changes are captured in regions near the peak stress the time step is reduced, however, it is possible the peak was reduced somewhat by too large a time step. From the analysis the maximum full-truss-equivalent stress was found to be 0.72 MPa. This value is identical to the value from the analytical prediction which suggests that the majority of the assumptions made in the purely analytical model are largely valid.

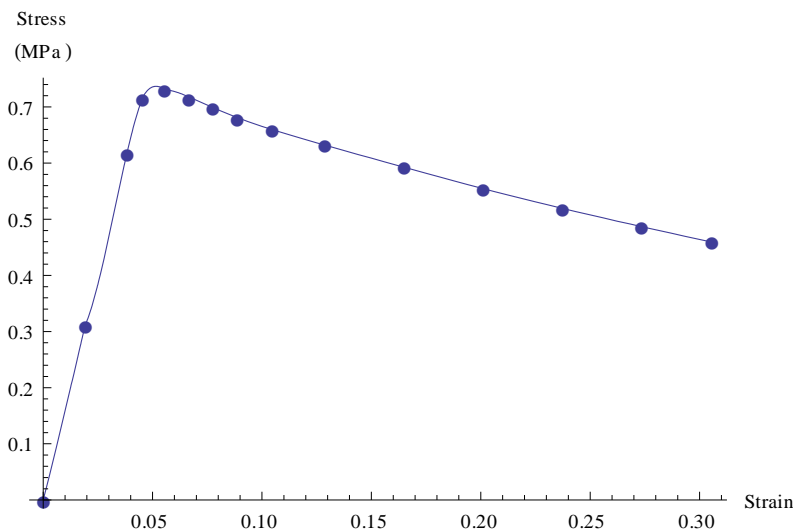


Figure 48: Stress-strain curve based on sum of top surface reaction forces and applied displacements to finite element model of single unit cell. The points represent individual time-points from the finite element analysis.

In addition to estimating the peak stress in the truss the finite element model can help understand the deformation which occurs in the model. Figure 49 shows the von Mises stress in the truss at the final

time-step of the analysis, corresponding to the maximum displacement of -0.3 mm in the z-axis. The deformed geometry is also evident in Figure 49, showing the buckling of the struts. The similarity between the finite element model's peak stress prediction and the peak stress predicted by the analytical model is fortuitous but not completely unexpected as the material property model for the polymer is identical in both the FE and the analytical model.

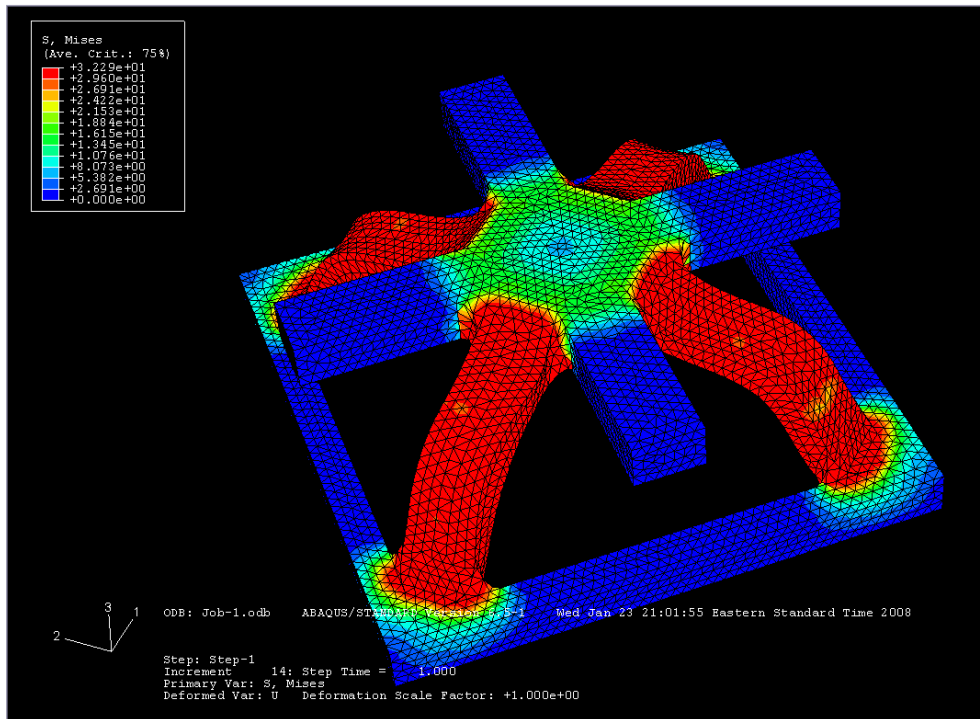


Figure 49: von Mises stress in single unit cell after application of a 0.3mm compressive displacement. The stress in the struts is equal to the yield stress of 32 MPa, note the extensive plastic deformation which occurs in the struts during compression.

Figure 48 captures many of the same phenomena as the experimental mechanical tests: the initial linear elastic deformation, the peak stress behavior during which the structure yields and then the post peak softening as the structure collapses. However, the final densification stage is not displayed in the finite element analysis. To model the densification the finite element model would need to account for contact stresses at the surfaces which come together during continued deformation.

5.6. Scaling Relations

One of the primary benefits of periodic cellular materials is that the compressive modulus and the peak stress of the truss are linear functions of density unlike traditional stochastic foams which scale nonlinearly with density (relative and actual) [2, 62]. The following relationships have commonly been used to describe the relationship between stiffness and strength and relative density for foams [62]

$$\frac{E^*}{E} = C_1 \left(\frac{\rho^*}{\rho} \right)^N \quad (24)$$

$$\frac{\sigma^*}{\sigma} = C_2 \left(\frac{\rho^*}{\rho} \right)^N \quad (25)$$

where E^* and E are the compressive elastic modulus of the foam and the parent material, respectively, σ^* and σ are the compressive elastic modulus of the foam and the parent material, respectively, C_1 and C_2 are empirical constants, and ρ^*/ρ is the relative density of the foam. For traditional foams N has been found to be equal to 2 while for PCMs the value is equal to 1 – representing a linear relationship [1, 2].

Based on the density of the constituent materials, polymer and nano-Ni, in the truss (Table 2) and their relative volume fractions the apparent density of the truss itself can be calculated as a function of the thickness of the electrodeposited nano-Ni. This relationship is illustrated below (Figure 50).

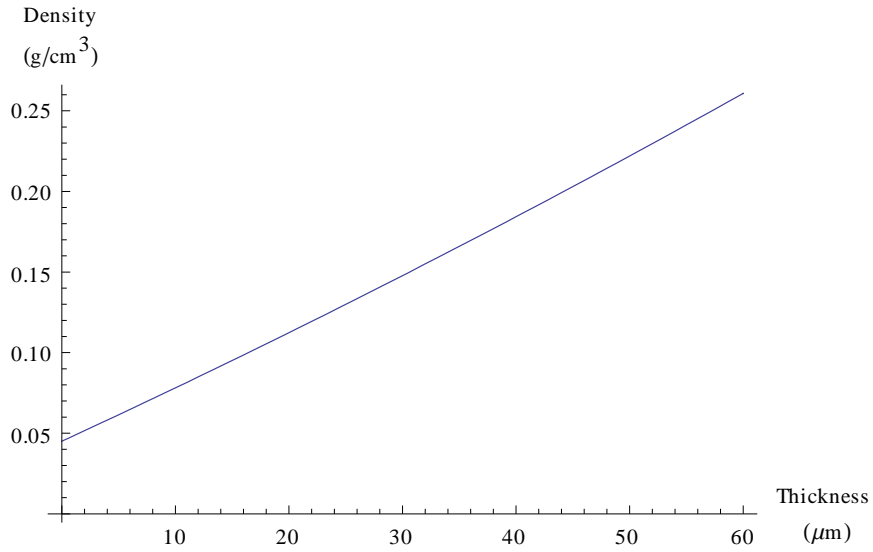


Figure 50: Apparent truss core density as a function of electrodeposited nano-Ni coating thickness.

Using the above relationship (Figure 50) the compressive modulus and peak compressive stress vs. coating thicknesses can be plotted as functions of density instead of a function of thickness illustrated in the following two figures.

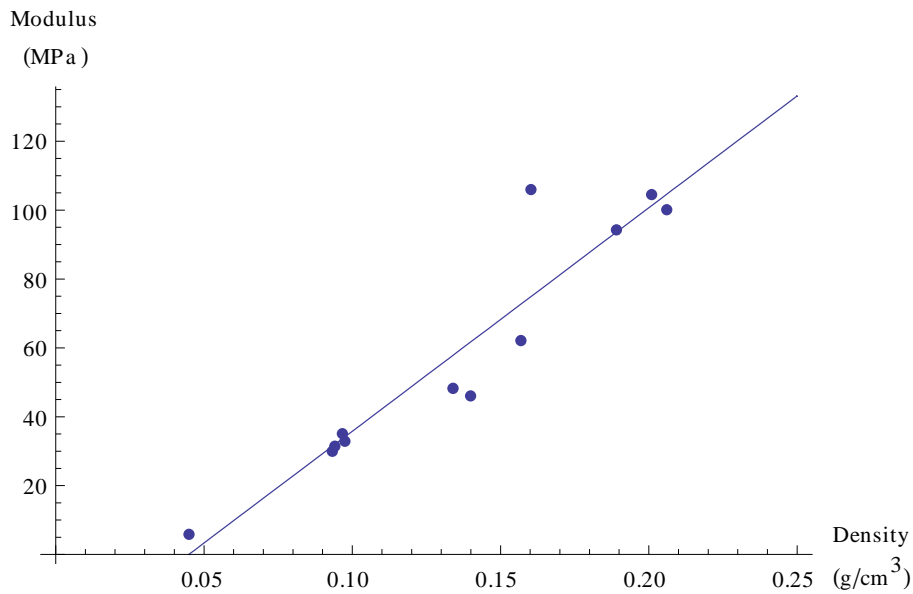


Figure 51: Compressive modulus plotted as a function of density, points plotted represent experimental measurements for all trusses, and the solid line represents the linear regression.

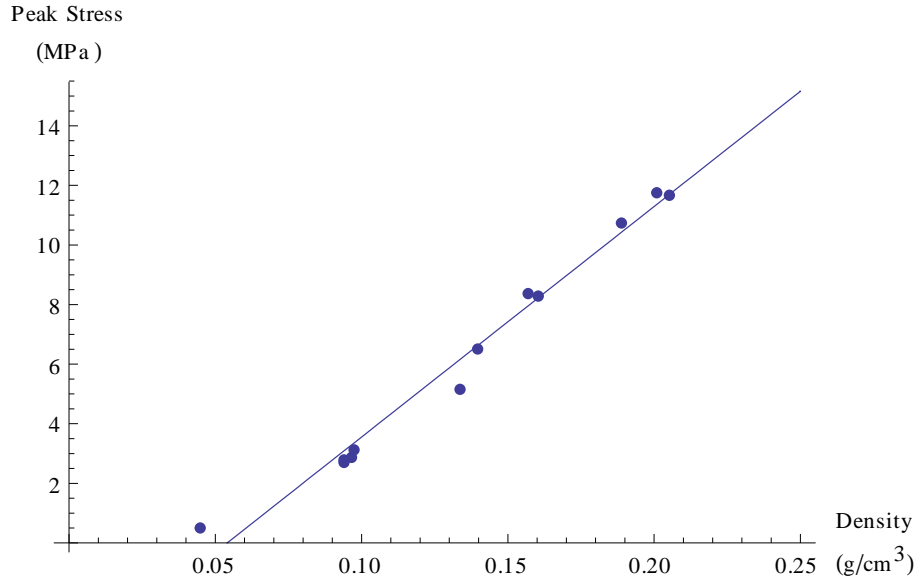


Figure 52: Peak compressive stress plotted as a function of density, points plotted represent experimental measurements for plated trusses, and the solid line represents the linear regression.

A linear regression was performed on each set of data. The estimated independent parameters from each linear regression ($y = mx + b$) and the associated R^2 values are listed in the following table (

Table 5).

Table 5: Estimated linear regression parameters and R^2 values.

| Linear Regression ($y = mx + b$) | Modulus (E) | Peak Stress (σ) |
|--|--------------------|--|
| Slope (m) | 649.08 | 77.37 |
| y-intercept (b) | -29.12 | -4.18 |
| R^2 | 0.89 | 0.98 |

The high R^2 values, 0.89 and 0.98 for the modulus and the peak stress, respectively, confirm the linear scaling relationship between the compressive modulus and the peak compressive stress of the trusses with density. It can be seen that the regression lines do not intersect with the origin, this is due to the composite nature of trusses and the fact that both materials have very different densities and mechanical properties (strength and stiffness).

Given this linear scaling relationship of these mesoscale PCMs it makes it possible to open up a wide new region of the material property space (Figure 4). Just in this small study densities ranging from 0.045 g/cm^3 to 0.206 g/cm^3 were created. Figure 3 shows the significantly higher specific stiffness of PCMs at lower relative densities when compared to stochastic foams. This linear scaling relationship has already been presented in the existing PCM literature [1, 56]. However, this is the first time that the relationship has been shown to extend down to sub-millimetre mesoscale PCMs. The linear scaling properties of the mesoscale PCM demonstrated here allows for the new regions of the material-property space to be made available to many new applications operating on a much smaller length scale than the PCMs presented so far.

5.7. Optimization

The truss developed here takes advantage of both structural and microstructural features to maximize the strength and stiffness of the truss while reducing its density. By combining these approaches the mechanical properties of the truss can be greatly improved. The trusses studied here are fabricated using a polymer template which is coated with a sleeve of high strength nanocrystalline nickel. The sleeve geometry is conceptually very similar to a hollow tube which has a greater structural efficiency than a solid rod. However, the polymeric substrate within the tube has very little strength but not zero density, it effectively acts as dead weight. This dead weight reduces the specific strength of the truss over the range of densities. If the polymer were removed by dissolution or an alternative method to form hollow nano-Ni tubes it would be possible to further optimize the mechanical properties of the truss. Removing the polymer reduces the density of the truss by 0.045 g/cm^3 . This allows more nanocrystalline nickel to be deposited for a given target density. The increased nickel results in an increase in effective strength of 2.4 MPa when comparing equal densities. Figure 53 illustrates this relationship.

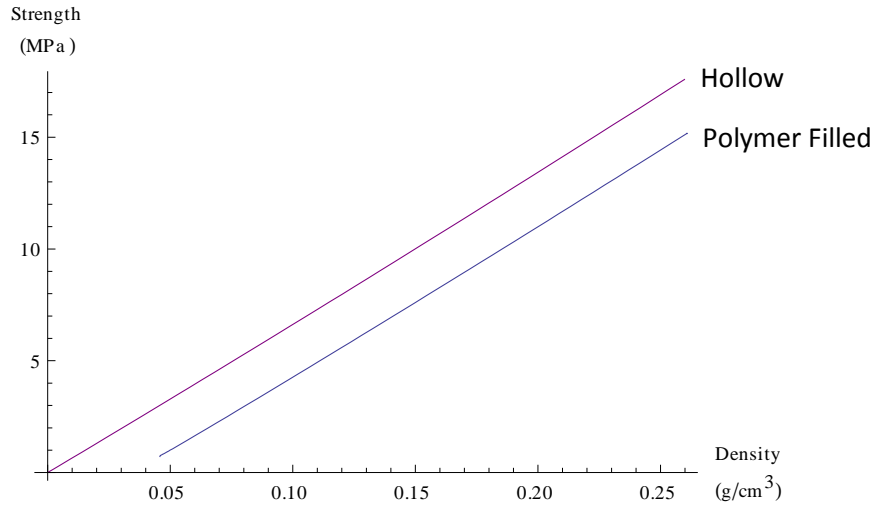


Figure 53: Comparison of strength of hollow struts compared to polymer filled struts – strength vs. density.

The hollow trusses provide a significant advantage over the polymer filled struts and by substituting the section properties of a solid nano-Ni rod into the analytical model developed here it becomes possible to compare the properties of a truss composed of solid rods with a truss here composed of tubes. The cross-sectional aspect ratio of the solid rod is 2.1 – approximately the same as aspect ratio of the hollow rectangular tubes over the range of thicknesses of nano-Ni plating. Figure 54 shows the strength vs. density relationship of a truss composed of solid rods or hollow tubes. The material properties of the nanocrystalline nickel are used. It can be seen that at a specific density the strength of the truss composed of tubes is higher than that of the truss composed of rods. However, if the wall thickness of the hollow strut is sufficiently thin the strut will fail instead by localized buckling at a lower stress instead of buckling due to global structural instability [46]. The onset of new failure modes needs to be considered when adjusting the geometry of the trusses.

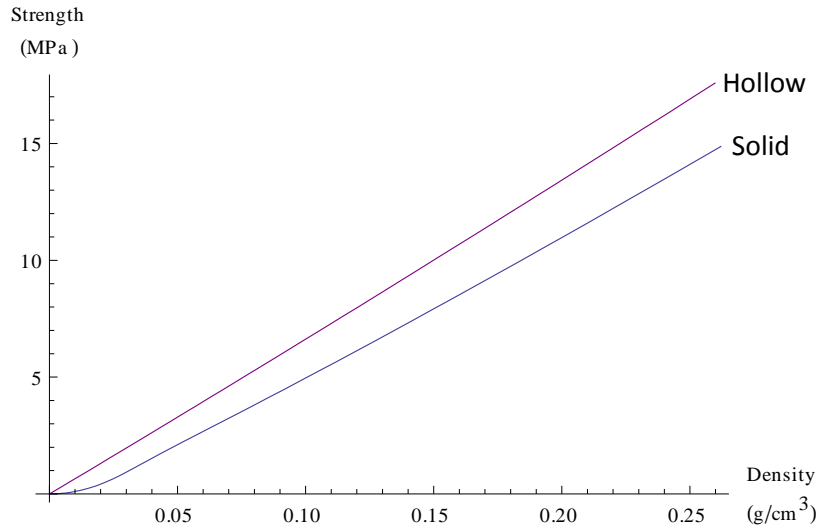


Figure 54: Comparison of strength vs. density for trusses constructed from hollow and solid struts.

The strut cross-section being studied here is rectangular with an aspect ratio of approximately 2.1. Reducing the aspect ratios of the strut cross-section would improve the properties of the truss. Figure 55 illustrates the effect of changing the strut cross-section aspect ratio on the strength vs. density relationship for trusses composed of solid struts. Hollow tubes would display a similar relationship. Note that an aspect ratio below 1 is impossible as the strut would then buckle in the thinner direction and the actual aspect ratio would be equal to the inverse of the aspect ratio below 1. The aspect ratio of unity corresponds to a square and for this truss the properties of circular struts are nearly identical to square struts.

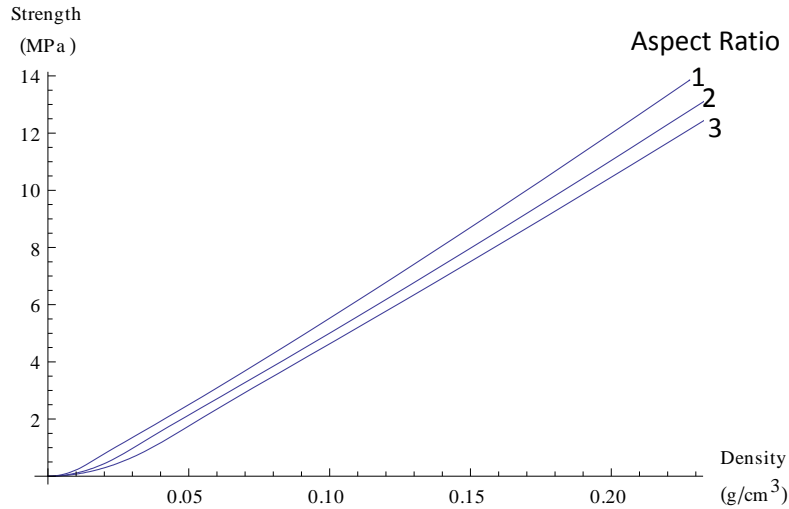


Figure 55: Illustrating the effect of strut cross-section aspect ratio for a truss composed of solid struts. Strength/density increases with decreasing aspect ratio.

Nanocrystalline nickel exhibits a significantly higher yield strength compared to conventional polycrystalline nickel. This increase in yield strength translates directly into an increased inelastic critical buckling load. Similar to the process used to compare the properties of a tube-truss to a rod-truss it is possible to substitute the material properties of conventional polycrystalline nickel ($E = 207 \text{ GPa}$, $\sigma_y = 183 \text{ MPa}$ [42]) in the analytical model and plot the new properties as a function of density for a range of plating thicknesses. The following figure illustrates this comparison. It can be seen that for each density the strength of the nanocrystalline nickel truss significantly exceeds the strength of the conventional polycrystalline nickel truss.

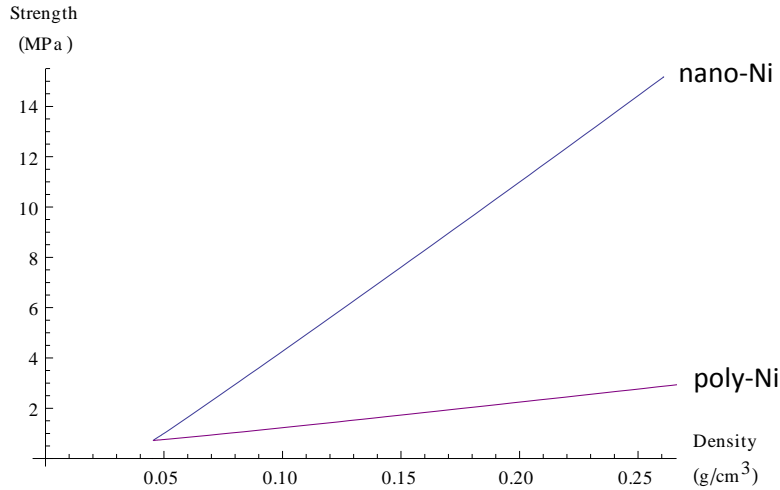


Figure 56: Truss strength as a function of density for nano-Ni and poly-Ni plating.

Overall, using electrodeposition to produce a hybrid polymer-Ni truss substantially increases not only the strength (from 0.5 to 11.8 MPa) and modulus (from 5.6 to 105.9 MPa) of the truss but the specific strength and specific modulus are also improved, from 10.9 to 58.6 MPa m³ Mg⁻¹ and from 125.2 to 661.7 MPa m³ Mg⁻¹, for the specific strength and the specific modulus, respectively. The relationship between specific strength (strength/density) as a function of plating thickness is illustrated in Figure 57 along with the theoretical prediction. The relationship between specific modulus (modulus over density) is similarly illustrated in Figure 58, however, the theoretically predicted modulus was reduced by an empirically derived constant knock-down factor. This new reduced modulus is given as

$$E(t)_{reduced} = \frac{E(t)}{k} \quad (26)$$

where k is the knock-down factor and $E(t)$ is the theoretically predicted truss modulus as a function of thickness. Fitting equation (26) to the experimental data gives a value for k of 5.8, this value indicates that the measured modulus values for the samples are on average only 17% ($1/5.8$) of the predicted value. Note that the outlying data point is slightly increasing the reduced modulus.

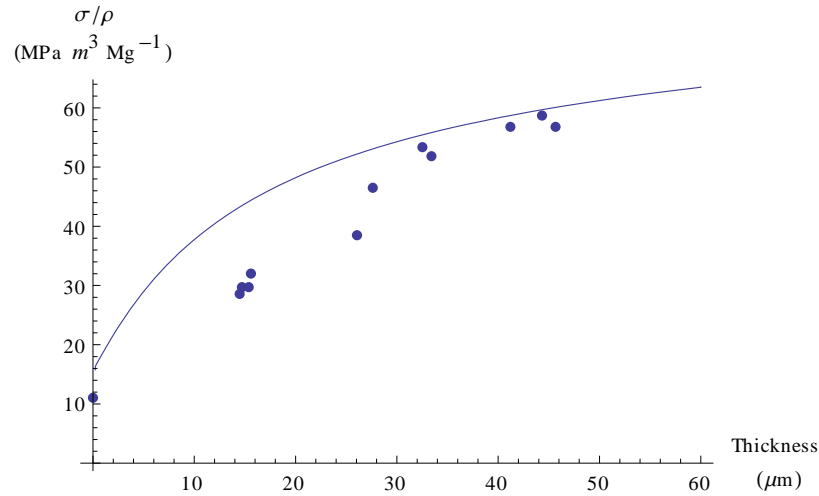


Figure 57: Specific strength plotted as a function of nano-Ni plating thickness. Individual points represent the experimental measurements and the continuous line is the theoretical prediction.

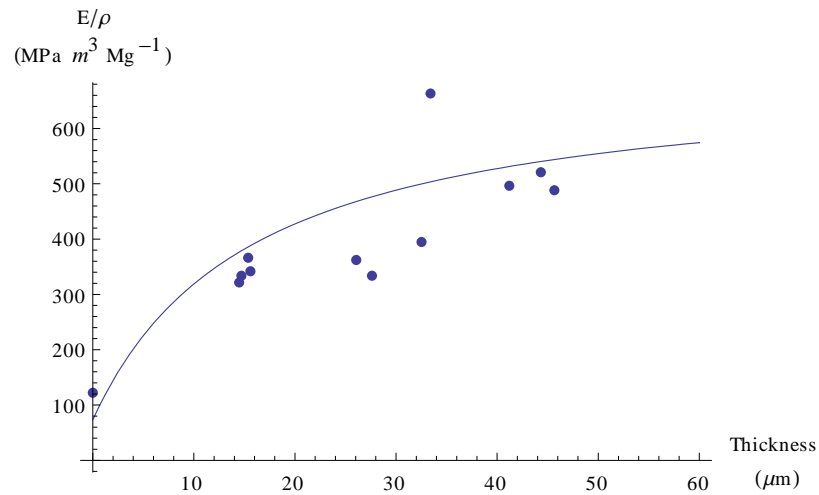


Figure 58: Specific modulus plotted as a function of nano-Ni plating thickness. Individual points represent the experimental measurements and the continuous line is the reduced theoretical modulus.

An understanding of the macrostructure-property and microstructure-property relationships of the composite polymer-nano-Ni mesoscale PCM truss developed here makes it possible to understand the benefits of this design over other trusses and traditional materials. This understanding also presents a means to optimize the physiomechanical properties of the truss for specific applications. Combining the improved properties with the linear property scaling and the mesoscale nature of the truss provides a wide range of possible properties and applications.

6. Future Work

This study investigated the relationship between the macro- and micro-structure and the compressive properties of a mesoscale PCM. The PCM was produced using a combination of multi-jet-modeling, a commercial rapid prototyping technology, and electrodeposition of nanocrystalline nickel. The rectangular strut geometry used for this study was selected to control the buckling mode and does not possess optimal specific strength. Reducing the aspect ratio of the strut towards a square or circular cross-section would increase the specific strength of the truss.

Rapid prototyping technologies provide an enormous amount of flexibility to the designer. By taking advantage of this flexibility, struts with non-uniform cross-sections along their length can be fabricated. Since the maximum resistance to buckling is needed in the middle of the strut, the majority of the mass should be concentrated there. This can be done using a cross-section which tapers outwards from each end towards the middle of the strut. Keller has analytically shown the improvements from using a tapered strut cross-section [63].

For this preliminary study only the compressive properties of the truss were investigated. Testing the strength of trussed-beams and columns loaded in bending and compression (buckling), respectively, along with the development of new analytical models will give further insight into the properties and the structure-property relationships of the mesoscale PCM. In addition, the shear properties of the truss could be investigated. Understanding more of the properties and having the ability to tailor them to meet the needs of specific applications will open up a range of diverse applications for the composite mesoscale PCM based on the possible properties which can be engineered.

This study evaluated the improvements made possible with structural and microstructural changes. The latter concept can be extended further by developing mesoscale trusses using higher performance materials which can also be deposited onto the rapid prototyped polymer substrate. Higher strength

nanocrystalline metals (ex. Ni-Fe alloys) could be electrodeposited instead of pure Ni to increase the specific strength. High thermal conductivity materials (ex. Cu) could also be used to create multi-functional PCMs for heat exchange and structural applications. Other methods of depositing high-strength materials, such as chemical vapor deposition (CVD), could also be investigated.

The finite element model developed in this study is relatively simple and relies on an idealized model of the polymer mechanical properties (as does the analytical model). It was explained in the analytical model development section that polymers can have quite different tensile and compressive properties. The best way to understand the compressive properties of the material would be to create a suitable sample of the polymer using the multi-jet-modelling approach and test the sample in compression. Furthermore, the finite element model was only used to investigate the mechanical properties of the as-received polymer truss. Extending the finite element model to include the nano-Ni/polymer composite truss would only require adjusting the CAD model to account for the electrodeposited nickel coating and then discretizing this new geometry to make the finite element mesh. The known material properties for the nickel would then need to be inputted into the FE model. The FE model also was not able to model the densification of the truss since self-contact between the various surfaces of the truss are not accounted for. By extending the model to simulate the densification the energy absorption of the truss could be investigated. An experimentally validated finite element model of the mesoscale truss would be very useful for engineering design purposes. The model could also be extended to account for other phenomena, such as heat transfer or high speed dynamic loading, to model multifunctional mesoscale PCMs in various situations.

7. Conclusion

The mesoscale PCM described here demonstrates the possibility of constructing a sub-millimetre scale truss using a combination of rapid prototyping to produce a polymer template and electrodeposition to

create a structural envelope of high-strength nano-crystalline nickel. The rapid prototyping technologies commercially available present a means of economically developing a template of various sizes, shapes and designs. Combining the rapid prototyped template with electrodeposited nanocrystalline nickel was demonstrated to be able to increase the strength by 24 times compared to the as-received polymer truss (from 0.5 to 11.8 MPa). The modulus was increased by a factor of 19 compared to the polymer truss (from 5.6 to 105.9 MPa). In addition the specific strength and specific modulus were also improved, from 10.9 to 58.6 MPa m³ Mg⁻¹ and from 125.2 to 661.7 MPa m³ Mg⁻¹, for the specific strength and the specific modulus, respectively. However, most importantly, the increase in density due to the addition of the nano-Ni sleeves is linearly proportional to the increase in strength and modulus. The linear scaling relationship opens up a completely new region of the material property space. Combining the new material properties accessible with the truss architecture and the sub-millimeter scale a multiplicity of new applications become possible. These applications range from biomedical devices to light-weight energy absorbing sheet metal alternatives.

Scanning electron microscopy (SEM) was used to observe both the as-received polymer trusses and the plated trusses. The plated trusses were imaged at several strain increments during a compression test. The first signs of damage to the truss, failure of some of nano-Ni sleeves over the face-sheet struts, occurred following the peak stress. Plotting the slope of the tangent of the stress-strain curve and looking for sharp negative spikes helped detect quick sharp drops in load – characteristic of cracking. The first of these spikes was found following the peak stress confirming the SEM observations.

To predict the properties of the truss it was first necessary to understand and model the mechanical properties of the constituent materials. For the rapid prototyping polymer the tensile elastic modulus and tensile strength were provided in the technical data sheet for the product. Since a full stress-strain curve was not available the polymer was assumed to be linearly elastic up to the tensile strength and

then perfectly plastic following the tensile strength when loaded in compression. For the nano-Ni a full stress-strain curve was available. The three parameter Ramberg-Osgood model was fit to the stress-strain curve and used to model the material in compression.

In order to use the stress-strain curve available for the nano-Ni it was necessary to confirm that the nickel deposited on the truss is nanocrystalline and that its mechanical properties match those of the sample tested. The average grain size of the electrodeposited nickel was measured to be 21.5 nm using x-ray diffraction by comparing the peak width to a polycrystalline standard. This measurement confirmed that the electrodeposited nickel is nanocrystalline (grain size < 100 nm) and that the mechanical properties are comparable.

By extending analytical models developed to describe conventional microtruss properties to the mesoscale composite truss it was possible to accurately predict the strength of the mesoscale PCM as a function of coating thickness. Coating thickness was measured for the plated samples based on the weight increase due to plating and the surface area of the sample. The plating thickness ranged from 15-45 μm . An understanding of the structure-property relationships for the new mesoscale truss makes it possible to optimize or calibrate the various material properties of the mesoscale PCM for specific applications. The compressive modulus was uniformly over predicted by 3.5 to 7 times for all the samples. This over prediction has been attributed to edge effects, transverse expansion and strut bending due to defects in the structure. The prediction of peak compressive stress for the truss was much more accurate, measured values ranged from 68 to 103% of the theoretical values. The over and under predictions have been attributed to inaccuracies in the material models used to describe the properties of the constituent materials and additional modes of deformation.

The analytical model developed here to predict truss properties was based on previous work which assumes all stresses and strains are transferred completely to the struts. This model fits well for large

truss cores with many unit-cells in all directions. This assumption is not always valid when the truss tested is relatively small, such as the sample tested here. Finite element analysis was used to produce a more relevant model of the experimental testing conditions. Using linear analysis of the entire polymer truss the modulus was calculated to be 13 MPa this estimate was much better than the analytically predicted value of 19.4 MPa and much closer to the experimentally measured value of 5.6 MPa. The remaining discrepancy is most likely due to defects in the truss causing bending of the struts. To determine the peak compressive stress a non-linear model of a single unit-cell was used. The peak stress was predicted to be 0.72 MPa, exactly the same as the analytical prediction, however, still 50% greater than the experimentally measured value.

References

- [1] Ashby, M. F. "Hybrids to fill holes in material property space," *Philosophical Magazine*, Vol. 85, 26-27, pp. 3235-3257, 2005.
- [2] Gibson, L. J and Ashby, M. F. *Cellular Solids*. Cambridge, UK : Cambridge University Press, 1997.
- [3] Wadley, Haydn N. G. "Cellular Metals Manufacturing," *Advanced Engineering Materials*, Vol. 4, 10, pp. 726-733, 2002.
- [4] Wadley, Haydn N. G. "Multifunctional Periodic Cellular Materials," *Philisophical Transactions of the Royal Society A*, Vol. 364, pp. 31-68, 2006.
- [5] Evans, A.G., Hutchinson, J. W. and Ashby, M. F. "Multifunctionality of cellular metal systems," *Progress in Materials Science*, Vol. 43, pp. 171-221, 1999.
- [6] Wadley, Haydn N. G., Fleck, Norman, A. and Evans, Anthony, G. "Fabrication and structural performance of periodic cellular metals and sandwich structures," *Composites Science and Technology*, Vol. 63, pp. 2331-2343, 2003.
- [7] Brittain, Scott T., et al. "Fabrication and Mechanical Performance of a Mesoscale Space-Filling Truss System," *Journal of Microelectromechanical Systems*, Vol. 10, 1, pp. 113-120, 2001.
- [8] Stampfl, J., et al. "Fabrication and moulding of cellular materials by rapid prototyping," *Int. J. Mat. Prod. Tech.* Vol. 21, 4, pp. 285-296, 2004.
- [9] Markaki, A. E. and Clyne, T. W. "Mechanics of thin ultra-light stainless steel sandwich sheet material," *Acta Materialia*, Vol. 51, pp. 1341-1350, 2003.
- [10] Li, Q., et al. "Mechanical Properties of Cast Ti-6Al-4V Lattice Block Structures," *Met. & Mat. Trans. A*, Vol. 39A, pp. 441-449, 2008.
- [11] Tari, G. "Gelcasting ceramics: A Review," *American Ceramics Society Bulletin*, Vol. 82, 4, pp. 43-46, 2003.
- [12] Kang, Ki Ju and Lee, Yong Hyun. "Three Dimensional cellular light structure directly woven by continuous wires and the manufacturing method of the same," World Intellectual Property Organization WO 2005/044483 A1, November 5, 2004.
- [13] Lim, Ji-Hyun and Kang, Ki-Ju. "Mechanical Behaviour of sandwich panels with tetrahedral and kagome truss cores fabricated from wires," *International Journal of Solids and Structures*, Vol. 43, pp. 5228-5246, 2006.
- [14] Fan, H. L., Meng, F. H. and Yang, W. "Mechanical behaviours and bending effects of carbon fiber reinforced lattice materials," *Archive of Applied Mechanics*, Vol. 75, pp. 635-647, 2006.
- [15] Lee, Yong-Hyun, et al. "Wire-woven bulk Kagome truss cores," *Acta Mat.* Vol. 55, 18, pp. 6084-6094, 2007.
- [16] van Vuure, A. W., Ivens, J. A. and Verpoest, I. "Mechanical properties of composite panels based on woven sandwich fabric preforms," *Composites A: App. Sci. Manuf.* Vol. 31, pp. 671-680, 2000.

- [17] Xia, Younan and Whitesides, George M. "Soft Lithography," *Annual Review of Materials Science*, Vol. 28, pp. 153-184, 1998.
- [18] Velev, Orlin D. and Lenhoff, Abraham, M. "Colloidal crystals as templates for porous materials," *Current opinion in colloid & interface science*, Vol. 5, pp. 56-63, 2000.
- [19] Ullal, Chaitany K., et al. "Photonic crystals through holographic lithography: Simple cubic, diamond-like, and gyroid-like structures," *Applied Physics Letters*, Vol. 84, 26, pp. 5434-5436, 2004.
- [20] Jang, Ji-Hyun, et al. "3D Polymer Microframes that exploit length-scale-dependent mechanical behaviour," *Advanced Materials*, Vol. 18, pp. 2123-2127, 2006.
- [21] Shoji, Satoru and Kawata, Satoshi. "Photofabrication of three-dimensional photonic crystals by multibeam laser interference into a photopolymerizable resin," *Applied Physics Letters*, Vol. 76, 19, pp. 2668-2670, 2000.
- [22] Hanemann, T., et al. "Rapid Prototyping and Rapid Tooling Techniques for the Manufacturing of Silicon, Polymer, Metal and Ceramic Microdevices," in *MEMS/NEMS: Handbook of Techniques and Applications*. Cornelius T. Leondes. New York, NY : Springer, 2006, pp. 187-200.
- [23] Chua, C. K., Leong, K. F. and Lim, C. S. *Rapid Prototyping: Principles and Applications*. Singapore : World Scientific Publishing, Co. Pte. Ltd., 2003.
- [24] Santorinaios, M., et al. "Crush behaviour of open cellular lattice structures manufactured using selective laser melting," *WIT Transactions on The Built Environment*, Vol. 85, pp. 481-490, 2006.
- [25] 3D Systems Inc. "Viper si2 SLA System," 2003.
- [26] Sobchak, Adam. Industrial Designer, Toronto Rehabilitation Institute: Intelligent Design for Adaptation, Participation and Technology (iDAPT). *Personal Communication*. November 8, 2007.
- [27] Haines, K. A. and Colburn, W. S. "Volume Hologram Formation in Photopolymer Materials," *Applied Optics*, Vol. 10, 7, pp. 1636-1641, 1971.
- [28] 3D Systems Inc. "InVision HR 3-D Modeler," 2007.
- [29] Palumbo, G., et al. "Nanotechnology opportunities for electroplating industries," *Plating and surface finishing*, Vol. 90, 2, pp. 36-45, 2003.
- [30] Gleiter, H. "Nanostructured Materials: Basic Concepts and Microstructure," *Acta Materialia*, Vol. 48, pp. 1-29, 2000.
- [31] Kadekar, Vinay, Fang, Weiya and Liou, Frank. "Deposition Technologies For Micromanufacturing: A Review," *Journal of Manufacturing Science and Engineering*, Vol. 126, 4, pp. 787-795, 2004.
- [32] Xu, B., Arias, F. and Whitesides, G. M. "Making honeycomb microcomposites by soft lithography," *Adv. Mater.* Vol. 11, 6, pp. 492-495, 1999.
- [33] Suralvo, M., et al. "Hybrid nanocrystalline periodic cellular materials," *Scripta Materialia*, Vol. 58, 4, pp. 247-250, 2008.
- [34] Ashby, M. F. *Materials Selection in Mechanical Design*. Oxford, UK : Butterworth-Heinemann, 2005.

- [35] Jacobsen, A., Barvosa-Carter, W. and Nutt, S. "Micro-scale truss structure formed from self-propagating photopolymer waveguides," *Adv. Mater.* Vol. 19, pp. 3892-3896, 2007.
- [36] Jacobsen, A. J., Barvosa-Carter, W. and Nutt, S. "Compression behaviour of micro-scale truss structures formed from self-propagating polymer waveguides," *Acta Mat.* Vol. 55, pp. 6724-6733, 2007.
- [37] Jacobsen, A., Barvosa-Carter, W. and Nutt, S. "Shear behaviour of polymer micro-scale truss structures formed from self-propagating polymer waveguides," *Acta Mat.* Vol. 56, pp. 1209-1218, 2008.
- [38] Bele, E., Bouwhuis, B. and Hibbard, G. D. "Work hardening as a strengthening mechanism in periodic cellular materials," *Mat. Sci. Eng. A*, Vol. in press, 2008.
- [39] Cheung, C., et al. "Electrodeposition of nanocrystalline Ni-Fe alloys," *Nanostructured materials*, Vol. 5, 5, pp. 513-523, 1995.
- [40] Ramberg, W. and Osgood, W. R. *Description of stress-strain curves by three parameters*. Washington DC. : National Advisory Committee For Aeronautics, 1943. Technical Note No. 902.
- [41] U.S. Forest Service Research Note. *A study on the strength of short and intermediate wood columns by experimental and analytical methods*. Madison, WS. : United States Department of Agriculture Forest Service, 1964. FPL-028.
- [42] Callister, William D. Jr. *Fundamentals of Materials Science and Engineering*. Second Edition. Hoboken, NJ : John Wiley & Sons, 2005.
- [43] Gad-el-Hak, Mohamed. *The MEMS Handbook*. Sound Parkway, NW : CRC Press, 2005.
- [44] Wei, Hung-Hsun. "Tensile properties of nanocrystalline Ni-Fe alloys," *Master's Thesis: University of Toronto*. 2006.
- [45] Desphande, V. S. and Fleck, N. A. "Collapse of truss core sandwich beams in 3-point bending," *Int. J. Solid. Struct.* Vol. 38, pp. 6275-6305, 2001.
- [46] Timoshenko, S. P. and Gere, J. M. *Theory of Elastic Stability*. New York, NY : McGraw-Hill, 1961.
- [47] Gere, James M., Timoshenko, Stephen P. *Mechanics of Materials*. Norwell, MA : Chapman & Hall, 1991.
- [48] Shanley, F. R. "Inelastic Column Theory," *J. Aeronautical Sci.* Vol. 14, 5, pp. 261-268, 1947.
- [49] Shanley, F. R. *Strength of Materials*. New York, NY : McGraw-Hill, 1957.
- [50] Bazant, Z. P. "Shear buckling of sandwich, fiber composite and lattice columns, bearings and helical springs: paradox resolved," *J. App. Mech.* Vol. 70, pp. 75-83, 2003.
- [51] Bazant, Zdenek, P. and Beghini, Alessandro. "Which formulation allows using a constant shear modulus for small-strain buckling of soft-core sandwich structures," *J. App. Mech.* Vol. 72, pp. 785-787, 2005.
- [52] Kardomateas, G. A. and Dancila, D. S. "Buckling of moderately thick orthotropic columns: comparison of an elasticity solution with the Euler and Engesser/Haringx/Timoshenko formulae," *Int. J. Sol. Struct.* Vol. 34, 3, pp. 341-357, 1997.

- [53] Rathbun, H. J., et al. "Measurement and simulation of the performance of a lightweight metallic sandwich structure with a tetrahedral truss core," *Trans. ASME*, Vol. 71, May, pp. 368-374, 204.
- [54] Hyun, S., et al. "Simulated properties of kagome and tetragonal truss core panels," *Int. J. Solids & Struct.* Vol. 40, pp. 6989-6998, 2003.
- [55] Lee, S., et al. "Dynamic failure of metallic pyramidal truss core materials - experiments and modeling," *Int. J. Plasticity*, Vol. 22, pp. 2118-2145, 2006.
- [56] Bouwhuis, B. and Hibbard, G. "Compression testing of periodic cellular sandwich cores," *Metallurgical Mat. Trans*, Vol. 37B, pp. 919-927, 2006.
- [57] Wallach, J. C. and Gibson, L. J. "Mechanical behaviour of a three-dimensional truss material," *Int. J. Solids Struct.* Vol. 38, pp. 7181-7196, 2001.
- [58] Kooistra, G. W. and Wadley, H. H. G. "Lattice truss structures from expanded metal sheet," *Mat. & Design*, Vol. 28, pp. 507-514, 2007.
- [59] Nielson, L. E. *Mechanical properties of polymers and composites, vol. 2*. New York, NY : Marcel Dekker, 1974.
- [60] Cheng, S., Spencer, J. A. and Milligan, W. W. "Strength and tension/compression asymmetry in nanostructured and ultrafine-grain metals," *Acta Mat.* Vol. 51, pp. 4505-4518, 2003.
- [61] El-Sherik, A. M., Shirokoff, J. and Erb, U. "Stress measurements in nanocrystalline Ni electrodeposits," *J. Alloys & Compounds*, Vol. 389, pp. 140-143, 2005.
- [62] Woesz, A., Stampfl, J. and Fratzl, P. "Cellular solids beyond the apparent density - an experimental assessment of mechanical properties," *Adv. Eng. Mat.* Vol. 6, 3, pp. 134-138, 2004.
- [63] Keller, Joseph B. "The shape of the strongest column," *Arch. rational Mech. Anal.* Vol. 5, pp. 275-285, 1960.
- [64] Overhults, Wendell C. "Cross-linked cyanoacrylate adhesive compositions," US Patent 3940362, February 24, 1976.
- [65] Kooistra, G. W., Deshpande, V. S. and Wadley, H. N. G. "Compressive behaviour of age hardenable tetrahedral lattice truss structures made from aluminum," *Acta Mat.* Vol. 52, pp. 4229-4237, 2004.
- [66] Wang, J., et al. "On the performance of truss panels with Kagome cores," *Int. J. Solids Struct.* Vol. 40, pp. 6981-6988, 2003.

Appendix A: Rapid Prototyping Datasheet

Technology

| | |
|----------------------------|--|
| Product | InVision®HR3-D Modeler system (InVision®HR3-D Modeler, software, VisiJet®material starter kit, warranty) |
| Modeler | InVision®HR3-D Modeler |
| Materials | Model material - VisiJet®HR200 Support material - VisiJet®S100 |
| Software | InVision print client software |
| Accessories (not included) | InVision Finisher |

Modeler

| | |
|-----------------------------|--|
| Technology | Multi-Jet Modeling (MJM). Thermal material application, with UV-curing |
| Maximum Build Volume | W127 x D178 x H50 mm (W5.0 x D7 x H2 in) (xyz) |
| Maximum Single Part Size | 64.5 cm ² (xy) x 5 cm (z); 10 in ² (xy) x 2 in (z) |
| Resolution | 656 x 656 x 800 DPI (xyz) |
| Certifications | UL certified, CE marked, CB certified |
| Electrical | 100-127 VAC, 50/60 Hz, single-phase, 15A; 200-240* VAC, 50 Hz, single-phase, 10A; IT Power System Specification Compliant (Nordic countries) |
| Operating Temperature Range | 18-28 °C (64-82 °F) |
| Noise | <60 dBA estimated (at medium fan setting) |
| Printer (Crated) (WDH) | 371 kg (817 lb) 0.96 x 1.42 x 1.67 m (38 x 56 x 66 in) |
| Printer (Uncrated) (WDH) | 254 kg (560 lb) 0.77 x 1.24 x 1.48 m (30 x 49 x 58 in) |

Interface

| | |
|--------------------------------|--|
| Network Compatibility | Network ready with 10/100 Ethernet interface |
| Client Hardware Recommendation | 1.8 GHz Pentium IV with 1 GB RAM (with OpenGL support and minimum 64 mb video RAM) or higher |
| Client Software OS Support | Windows XP Professional/2000/NT 4.0/Me/98 |
| Input Data File Format | .stl; .slc |

Materials

| Material | Model | Support |
|---|------------------------|----------------|
| | VisiJet®HR200 | VisiJet®S100 |
| Composition | Acrylic plastic | n/a |
| Color | Blue | White |
| Case Quantity | 4 cartridges | 8 cartridges |
| Net Weight (Approximate)** | 500 g (1.1 lb) | 405 g (0.9 lb) |
| Density @80 °C (ASTM D4164) | 1.02 g/cm ³ | n/a |
| Tensile Modulus (ASTM D638) | 1724 MPa (250 KSI) | n/a |
| Tensile Strength (ASTM D638) | 32 MPa (4.7 KSI) | n/a |
| Tensile Elongation at Break (ASTM D638) | 12.3% | n/a |
| Flexural Modulus (ASTM D790) | 1551 MPa (225 KSI) | n/a |
| Flexural Strength (ASTM D638) | 45 MPa (6.6 KSI) | n/a |

ASTM protocol followed for testing, except RH conditioning, which is not expected to substantially affect results.

* Requires a small external transformer (pn 23418-901-00); supplied by 3D Systems in the country kit.

** Weights and dimensions are estimated, nominal values and subject to change without notice. Accessory kit shipped separately.

Appendix B: Wire Pre-form

A woven or sewn wire pre-form was constructed by first drilling a specific repeating pattern into a rectangular 1mm thick 3003 aluminum alloy sheet (McMaster-Carr, Los Angeles, CA) with a 353 μ m diameter (#80) cobalt-steel drill bit (McMaster-Carr, Los Angeles, CA). The top and bottom face-sheets were connected with #4 $\frac{3}{4}$ " long 18-8 stainless steel bolts and 3/16" diameter low profile 18-8 stainless steel nuts (McMaster-Carr, as before), one bolt and nut in each corner of the sheet. The correct distance between the face-sheets was maintained using a 3/16" hollow aluminum spacer (McMaster-Carr, as before) placed over each of the bolts. A 150 μ m diameter steel wire was then anchored to one of the holes in the bottom face-sheet by tying an overhand knot in the wire before feeding it through the lower hole. The wire was then fed through the corresponding hole in the top face-sheet where it was tensioned and anchored in place using 3M Scotch-Weld CA-7 cyanoacrylate adhesive (3M Company, Maplewood, MN). Before feeding the wire through the top hole a drop of a 3M Scotch-Weld Instant Adhesive Surface Activator (solution of N,N-dimethyl-p-toluidine dissolved in acetone) (3M Company, as before) was placed around the hole. The acetone evaporated leaving the N,N-dimethyl-p-toluidine on the metal surface which catalyzes the polymerization of the cyanoacrylate adhesive [64]. Following curing of the adhesive excess length of wire was removed using angle cutters.

For wire pre-form fabrication a Kagomé lattice (Figure 5c) was selected as the Kagomé lattice eliminates the need for a wire to pass through a single hole twice, reducing the necessary size of the hole and simplifying the weaving procedure. Kagomé lattice face-sheet templates (Figure 59) and 3D rendering of the wire perform (Figure 60) are shown to scale below (calculated and rendered using Mathematica 6.0.1.0, Wolfram Research, Champaign, IL).

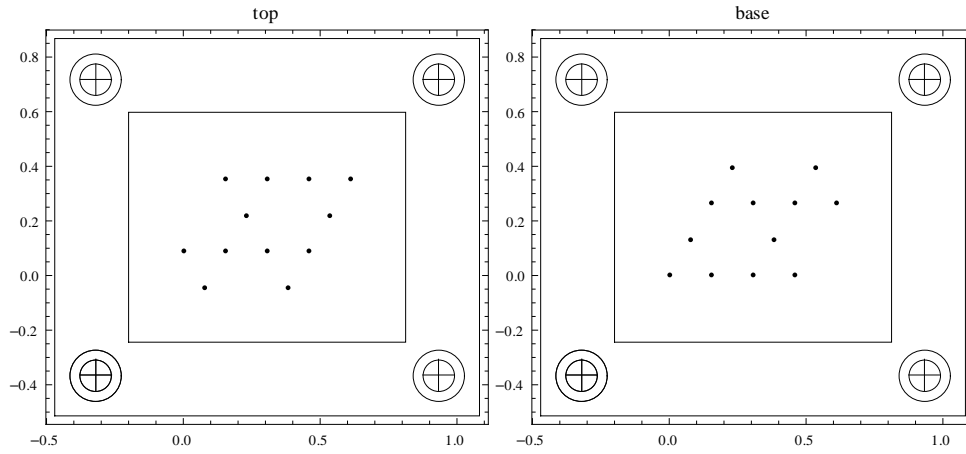


Figure 59: 2x2 Kagome Lattice Face-sheet drilling templates.

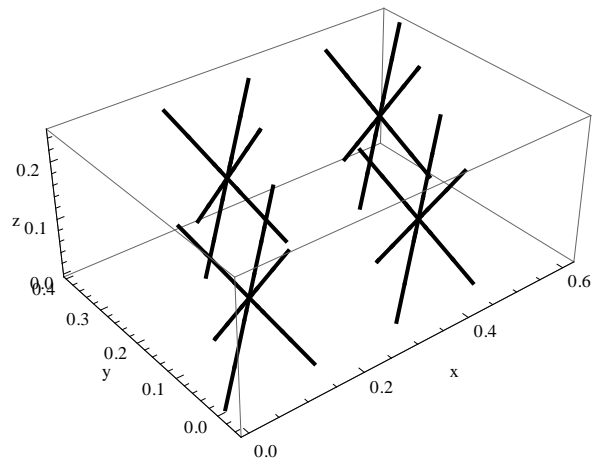


Figure 60: 2x2 Kagome Lattice Rendering

Appendix C: Transverse shear corrected buckling stress

The Engesser formula is most accurate for soft-core sandwich columns, it is given as

$$\bar{\sigma}_s = \frac{P_{cr}}{A_{tot}} = \frac{1}{A_{tot}} \left(\frac{P_E}{1 + (P_E/GA')} \right) \quad (27)$$

where P_E is the Euler critical buckling load, G is the shear modulus and A' is the effective area (where $A' = kA$ and k is the Timoshenko shear correction factor, approximately unity for this core/sleeve structure [50]). The average stress is then given as

$$P_{cr} = \frac{P_E}{1 + (P_E/GA')} \quad (28)$$

Since the modulus and the moment of inertia of the nano-Ni sleeve is much greater than the modulus of the polymer core it can be assumed that the entire axial load is carried by the nano-Ni, therefore

$$EI = E_{Ni}I_{Ni} \quad (29)$$

where I_{Ni} is the moment of inertia for a hollow rectangular section, given as a function of thickness in mm,

$$I(t)_{Ni} = \frac{b_2 h_2^3 - I_{poly}}{12} \quad (30)$$

For the shear stiffness of the structure it is not possible to simplify the expression, therefore a rule of mixtures approach will be used for the shear stiffness of the composite (an isostrain assumption is not required as the shear modulus of the polymer is unchanging and does not depend on the stress or strain)

$$GA_{tot} = G_{Ni}kA_{Ni} + G_{poly}kA_{poly} \quad (31)$$

where GA_{tot} is the shear stiffness of the strut and G_{Ni} and G_{poly} are the shear moduli of the nano-Ni and the polymer, respectively. The polymer it is assumed to be linearly elastic and spherically isotropic (note

that it was confirmed mathematically during the analysis that the stress in the polymer was below the tensile strength), therefore, the shear modulus is given by

$$G = \frac{E}{2 + 2\nu} \quad (32)$$

where ν is the Poisson's ratio. Substituting in the elastic modulus (1.724 GPa) and the Poisson's ratio for acrylic photopolymer (0.4, based on polymethylmethacrylate PMMA – assumed to be the same for the acrylic polymer used for rapid prototyping [43]) into equation (32) gives $G_{\text{poly}} = 621.4$ MPa.

Similarly, the nano-N is assumed to be spherically isotropic, however, instead of being modeled as a linearly elastic material, it is assumed that the shear modulus will vary with stress along with the tangent modulus described by equation (26). Substituting the tangent modulus equation (26) and the Poisson's ratio for nickel (0.31 [42]) into equation (32) gives the shear modulus for the nano-Ni as a function of stress in the material

$$G(\sigma)_{Ni} = \frac{1}{2 + 2\nu} \left(\frac{500E\sigma}{500\sigma + En \left(\frac{\sigma}{\sigma_0} \right)^n} \right) \quad (33)$$

Combining the above equations and the constituent material properties (Table 2) gives a system of equations describing the peak stress over the entire truss as a function of plating thickness, where $t > 0$,

This set of equations was solved numerically for each thickness using Mathematica 6.0.1.0 (Wolfram Research, as before) to determine the peak stress the over the truss as a function of thickness.